MASTERARBEIT / MASTER'S THESIS

Titel der Masterarbeit / Title of the Master's Thesis

„Experimental single-copy entanglement distillation“

verfasst von / submitted by

Philipp Vincent Sohr

angestrebter akademischer Grad / in partial fulfilment of the requirements for the degree of

Master of Science (MSc)

Wien, 2021 / Vienna, 2021

Studienkennzahl lt. Studienblatt / degree programme code as it appears on the student record sheet:	UA 066 876
Studienrichtung lt. Studienblatt / degree programme as it appears on the student record sheet:	Masterstudium Physik UG2002
Betreut von / Supervisor:	emer. o. Univ.-Prof. Dr. DDr. h.c. Anton Zeilinger
Mitbetreut von / Co-Supervisor:	

Abstract

Distributed entanglement is a vital and exclusive resource for many quantum communication protocols. Since remote parties cannot create shared entanglement using local operations and classical communication (LOCC) alone, parts of entangled quantum states must be sent via quantum channels. However, due to inevitable interaction with the environment during transmission, the entanglement is degraded and thus the security of quantum communication is compromised. One strategy to restore the quality of entanglement between two parties is entanglement distillation. By LOCC the entanglement of an ensemble of quantum states can be enhanced at the cost of the number of states.

In this thesis, entanglement distillation of photon pairs entangled in both, the energy-time degree of freedom (DOF) and the polarisation DOF independently, is demonstrated in a proof of principle experiment using passive linear optics only. This is the first photonic implementation that strictly follows the original proposal, with a polarising beam splitter efficiently acting as deterministic controlled NOT gate between the two employed DOF. Moreover, by employing hyperentanglement, the probability of success per photon pair sent is doubled compared to the original proposal. It is demonstrated, that various contributions of distinct noise models can be introduced independently in the two DOF. The high demands of interferometric stability are met and so an ensemble with a bit flip error in the polarisation DOF and a bit and bit-phase flip error in the energy-time DOF is successfully distilled. The results are consistent with the predictions of the developed theoretical model.

Because entanglement distillation is one of the building blocks of a quantum repeater, the results of this work are of great importance for the distribution of entanglement over long distances and a future quantum world wide web connecting quantum computers.

Kurzdarstellung

Verteilte Verschränkung ist eine wichtige und exklusive Ressource für viele Quantenkommunikationsprotokolle. Entfernte Parteien können mit lokalen Operationen und klassischer Kommunikation alleine keine geteilte Verschränkung erzeugen, sondern Teile von verschränkten Quantenzuständen müssen über Quantenkanäle gesendet werden. Aufgrund der unvermeidlichen Interaktion mit der Umgebung während der Übertragung wird die Verschränkung jedoch verschlechtert und damit die Sicherheit der Quantenkommunikation beeinträchtigt. Eine Strategie zur Wiederherstellung der Qualität der Verschränkung zwischen zwei Parteien ist die Verschränkungsdestillation. Mit gemeinsamen, aber lokalen Operationen und klassischer Kommunikation kann die Verschränkung eines Ensembles von Quantenzuständen auf Kosten der Anzahl der Zustände verbessert werden.

In dieser Arbeit wird die Verschränkungsdestillation von Photonenpaaren, die sowohl im Energie-Zeit-Freiheitsgrad als auch im Polarisationsfreiheitsgrad unabhängig voneinander verschränkt sind, in einem Machbarkeitsexperiment unter ausschließlicher Verwendung passiver linearer Optiken demonstriert. Dies ist die erste photonische Implementierung, die strikt dem ursprünglichen Versuchvorschlag folgt, wobei ein polarisierender Strahlteiler effizient als kontrolliertes NOT-Gate zwischen den beiden verwendeten Freiheitsgrade fungiert. Außerdem wird durch den Einsatz von Hyperverschränkung die Erfolgswahrscheinlichkeit pro gesendetem Photonenpaar im Vergleich zum ursprünglichen Vorschlag verdoppelt. Es wird gezeigt, dass verschiedene Beiträge unterschiedlicher Störungsmodelle unabhängig voneinander in die beiden Freiheitsgrade eingebracht werden können. Die hohen Anforderungen der interferometrischen Stabilität werden erfüllt und so wird ein Ensemble mit einem Bit-Flip Fehler in dem Polarisations Freiheitsgrad und einem Bit- und Bit-Phasen-Flip Fehler in dem Energie-Zeit Freiheitsgrad erfolgreich destilliert. Die Ergebnisse sind konsistent mit den Vorhersagen des entwickelten theoretischen Modells.

Da die Verschränkungsdestillation einer der Bausteine eines sogenannten Quanten-Repeaters ist, sind die Ergebnisse dieser Arbeit von großer Bedeutung für die Verteilung von Verschränkung über große Distanzen und ein zukünftiges Quanten-World-Wide-Web, das Quantencomputer untereinander vernetzt.

Table of Contents

1 Introduction

By harnessing fragile quantum states, quantum information processing can outperform classical information processing on relevant tasks. On the one hand, quantum algorithms like Grover's search [1, 2] and Shor's factoring [3, 4] offer up to exponential speedup compared to the best known classical algorithms. Thereby, they threaten widespread classical encryption techniques relying on computational assumptions. But quantum information offers both the problem and its solution. While quantum computing threatens secure communication, quantum communication, on the other hand, promises unconditional security. One of the most mature quantum technologies is quantum key distribution, but practical challenges remain [5]. Not only is the key rate much lower than in the classical case, but also the distance that can be bridged is limited. The distance is limited by noise due to the interaction of the quantum state with the environment during transmission.

Unlike classical states, arbitrary unknown quantum states cannot be copied [6]. While this is a fundamental pillar for the security of quantum communication, it is a challenge for communication over noisy quantum channels. As noise is always present in real quantum channels due to interactions with the environment, strategies to protect the quantum information carried by the quantum state are required. One strategy is quantum error correction. The state to be protected is embedded in a larger Hilbert space by redundantly encoding one logical qubit in multiple physical qubits [7]. Another strategy uses entanglement distillation [8, 9] and quantum teleportation [10, 11]. The task of sending an arbitrary unknown state is reduced to sending a specific known, entangled state. As long as the received state contains sufficiently large contributions of the original state, the sent state can be restored by distillation. In this way, maximally entangled states can be distributed, which are a resource for many quantum information processing protocols. With quantum teleportation, maximally entangled states can be used to simulate a noiseless quantum channel. Over long distances and especially noisy channels, this can still be applied by splitting the quantum channel in parts and use quantum repeaters in between [12]. Quantum repeaters in turn, consist of nested entanglement distillation and entanglement swapping [13] and the resource costs scale polynomially with the total distance bridged.

Here, a proof of concept entanglement distillation experiment using passive linear optics and photon pairs entangled in both, the polarisation and the energy-time degree of freedom independently is presented. The use of hyperentanglement, that is entanglement in multiple degrees of freedom simultaneously, not only enables the implementation of a deterministic controlled NOT gate with linear optics, but also halves the number of photon pairs required per distillation step. The success probability is at least doubled with respect to schemes not taking advantage of hyperentanglement.

At this point a note on terminology seems appropriate. A commonly used term for what is called here entanglement distillation is entanglement purification. The latter was coined by some of the early works [8, 14]. However, the term purification is used by theorists for a different concept [7]. To avoid confusion, the descriptive term distillation is used here instead, which also dates back to 1996 [15]. Other terms such as entanglement concentration [16] and filtering [17] are used for protocols with a similar goal but different approaches.

In section 2, basic relations and formalisms that are used throughout this work are briefly introduced. This includes the formal description and the geometric representation of quantum states in general and entangled states in particular. The Jones formalism used in the theoretical part of the work is introduced. Relevant for the experimental part of the work are the connection between Bell state fidelity and visibility as well as the statistics of single photon counting. In section 3, the generation of hyperentangled photon pairs is addressed. The process of spontaneous parametric down conversion is introduced in general. Specifically, the source configuration used in the experiment is discussed. Both polarisation degree-of-freedom entanglement and energy-time degree-of-freedom entanglement are generated. It is explained how the latter can be analysed with a Franson interferometer. Furthermore, the formal description of hyperentanglement is introduced and examples of its use are given. A motivation of entanglement distillation and a brief history of entanglement distillation protocols as well as a summary of photonic experiments performed so far is given in section 4. In section 5 the author's own contribution to the experiment performed throughout this masters project is discussed in detail. This includes the basic conception of the experiment, in particular the implementation of the precisely controlled introduction of noise in both degrees of freedom. The mathematical model developed by the author specifically for this experiment was used to implement a simulation with Wolfram Mathematica. This simulation allows the model and the performance of the single-copy entanglement distillation scheme to be illustrated with clear examples. The difference between the ideal model and the experimental reality is indicated and it is discussed how the model is adapted to close this gap. The experimental implementation is then presented and important steps of the alignment procedures are described. It is explained how the Bell state fidelity is determined experimentally and the corresponding configurations of the experimental setup are shown. In section 6 the results of the experiment are presented and compared with the simulation. Differences and matches between the simulation and experimental data is discussed. The conclusions of this work and an outlook to possible future experiments is given in section 7.

2 Basics

In this section a brief overview over the most relevant basics necessary to understand the later sections of this work is given. More thorough treatments can be found in textbooks such as by Cohen-Tannoudji et al [18], by Nielsen and Chuang [7] or by Barnett [19].

2.1 Pure and mixed quantum states

Quantum systems in a pure state can be described by a state vector

$$|\psi\rangle = \sum_n |\phi_n\rangle \langle\, \phi_n \,|\, \psi \,\rangle = \sum_n c_n |\phi_n\rangle \,, \tag{2.1}$$

that is a coherent superposition of states of an orthonormal basis $\{|\phi_n\rangle\}$ in a Hilbert space $\mathscr{H}$. State vectors are normalised, such that

$$|\langle\, \psi \,|\, \psi \,\rangle| = \sum_n |c_n|^2 = 1 \,, \tag{2.2}$$

and allow to compute probabilities for the outcomes of the measurement of an observable. Observables are described by hermitian operators. The possible measurement outcomes of an observable A are given by the eigenvalues of the operator a_n. For non-degenerate eigenvalues there is just one eigenvalue corresponding to one eigenvector

$$A|u_n\rangle = a_n|u_n\rangle \,. \tag{2.3}$$

When an operator A is applied to a system in state $|\psi\rangle$, the probability of obtaining outcome a_n is

$$\mathrm{p}\,(a_n) = |\langle\, u_n \,|\, \psi \,\rangle|^2 = \langle\, \psi \,|\, u_n \,\rangle \langle\, u_n \,|\, \psi \,\rangle \ , \tag{2.4}$$

where $|u_n\rangle\langle u_n| = P_{u_n}$ is the projector on the $|u_n\rangle$ state. The description of a pure state contains the full knowledge about the state. This means that the measurement outcome can be predicted with certainty provided the state of the system is an eigenstate of the applied operator. In this case the measurement outcome equals the corresponding eigenvalue with unit probability, while outcomes corresponding to the other eigenstates occur with probability zero. But if the system is not in an eigenstate of the measured observable, there is no unit probability to obtain a certain outcome, but the outcome is probabilistic. This randomness is not due to a lack of knowledge about the state, but rather due to the basis choice for the measurement. When there is a lack of knowledge about the state of a system, the state is called mixed and the best possible description is a statistical, incoherent mixture of pure states. Equivalent to the state vector description, but more convenient for mixed states, is the density matrix formalism. With this, a mixed state can be represented by the weighted sum of pure states $|\psi_i\rangle$

$$\rho = \sum_{i=1} p_i |\psi_i\rangle \langle\psi_i| \,, \tag{2.5}$$

where the weight p_i is the probability to find the system in the pure state $|\psi_i\rangle$. The probabilities $p_i \geq 0$ are non-negative and sum up to one, $\sum p_i = 1$. The description of a mixed quantum state by the density matrix is not unique. However, mixed states that can be described by the same density matrix cannot be distinguished from each other. The probability of obtaining outcome a_n when the projector P_{u_n} is applied can be easily computed like

$$p\left(a_n\right) = \mathrm{tr}\left\{P_{u_n} \rho\right\} \,. \tag{2.6}$$

More comprehensive introductions to the formalism of quantum theory can be found in textbooks such as [18] or [20].

An intuition for quantum state spaces can be supported by geometrical representations [21]. Quantum state spaces are strictly convex. The pure states are located on the extremal boundary and the mixed state in the convex hull as linear combinations of pure states.

For qubits, that are two-levels systems, the state space is a three dimensional ball, known as the Bloch ball. Orthogonal states are always vis-à-vis and per definition the states of the computational basis $\{|0\rangle, |1\rangle\}$ are located at the poles of the sphere. In Figure 2.1 the Bloch ball is depicted. The labels indicate the three bases for the polarisation of photons. The linearly polarised horizontal and vertical states $|\mathrm{H}\rangle$ and $|\mathrm{V}\rangle$ are located at the poles. The other linear polarisation basis $\{|\mathrm{D}\rangle, |\mathrm{A}\rangle\}$ and the circular polarisation basis $\{|\mathrm{R}\rangle, |\mathrm{L}\rangle\}$ are located at the equator.

The state vector of pure states on the Bloch sphere

$$|\psi\rangle = \cos\frac{\theta}{2}|0\rangle + \mathrm{e}^{\mathrm{i}\,\varphi} \sin\frac{\theta}{2}|1\rangle \,, \tag{2.7}$$

is parameterised by the azimuthal angle φ and the polar angle θ. With the representation

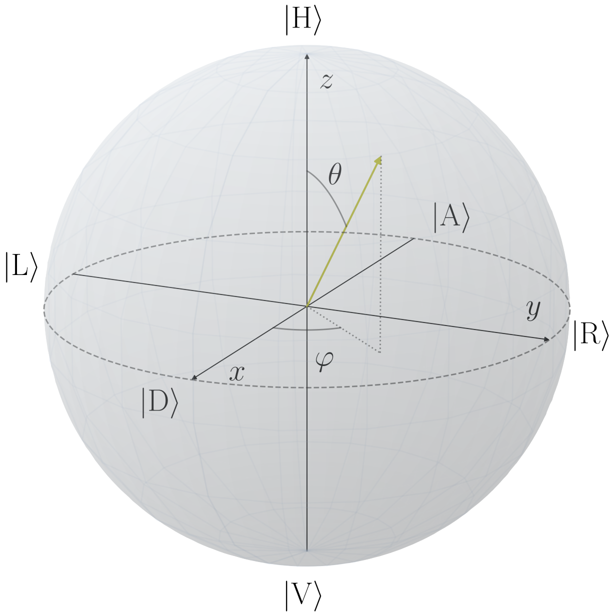

Figure 2.1: *Geometric representation of the qubit state space, known as Bloch ball. The labels refer to the polarisation states of photons. As an example, a pure state represented by a vector of unit length pointing on the surface of the ball and its parameterisation with the azimuthal angle φ and the polar angle θ is sketched. Mixed states are described by vectors of less than unit length pointing to the inside of the Bloch ball. In the course of this work, the axes labels are used to refer to the bases. The* x*-axis for the* D/A*-basis, the* y*-axis for the* R/L*-basis and the* z*-axis for the* H/V*-basis. This is not only shorter, but offers the benefit, that different degrees of freedom can be described with the same labels.*

$|\mathrm{H}\rangle = (1,0)^{\mathrm{T}}$ and $|\mathrm{V}\rangle = (0,1)^{\mathrm{T}}$, the corresponding density matrix is

$$\rho^{(1)}_{\text{Bloch}} = \begin{pmatrix} \cos^2\frac{\theta}{2} & \mathrm{e}^{-\mathrm{i}\,\varphi}\cos\frac{\theta}{2}\sin\frac{\theta}{2} \\ \mathrm{e}^{\mathrm{i}\,\varphi}\cos\frac{\theta}{2}\sin\frac{\theta}{2} & \sin^2\frac{\theta}{2} \end{pmatrix} \tag{2.8a}$$

$$= \frac{1}{2}\begin{pmatrix} 1+\cos\theta & \cos\varphi\sin\theta - \mathrm{i}\,\sin\varphi\sin\theta \\ \cos\varphi\sin\theta + \mathrm{i}\,\sin\varphi\sin\theta & 1-\cos\theta \end{pmatrix} \tag{2.8b}$$

$$= \frac{\mathbb{1}_2 + \mathbf{r}\cdot\boldsymbol{\sigma}}{2}\,, \tag{2.8c}$$

with the unit Bloch vector $\mathbf{r} = \cos\varphi\sin\theta\,\mathbf{e_x} + \sin\varphi\sin\theta\,\mathbf{e_y} + \cos\theta\,\mathbf{e_z}$ and the Pauli vector $\boldsymbol{\sigma} = \sigma_{\mathrm{x}}\mathbf{e_x} + \sigma_{\mathrm{y}}\mathbf{e_y} + \sigma_{\mathrm{z}}\mathbf{e_z}$, where $\mathbf{e_x}$, $\mathbf{e_y}$ and $\mathbf{e_z}$ are the unit vectors in x, y and z direction respectively. Mixed states are described by non-unit Bloch vectors pointing inside the Bloch ball. The decomposition of a mixed state is not unique, but there is always a basis that allows a diagonal representation. The representation of the maximally mixed state is the same in every basis. It is located at the origin of the Bloch ball, so the corresponding Bloch vector is the null vector and the density matrix is the identity matrix $\mathbb{1}_2/2$ [7].

2.2 Entangled states

The state space of composite quantum systems is the tensor product of the respective individual Hilbert spaces. In such spaces there exist peculiar states that are not tensor products of elements of the individual Hilbert spaces. In other words, there are composite states that cannot be separated into a tensor product of states from the Hilbert spaces of the subsystems. Such non-separable states are called entangled [22, 23].

The Bloch representation (eq. (2.8)) can be extended to two-qubit states. A product state of systems A and B is then written as

$$\rho^{(2)}_{\text{Bloch}} = \rho_{\mathrm{A}} \otimes \rho_{\mathrm{B}} = \frac{1}{4}\left(\mathbb{1}_2 + a_i\sigma_i\right)\otimes\left(\mathbb{1}_2 + b_j\sigma_j\right) \tag{2.9a}$$

$$= \frac{1}{4}\left(\mathbb{1}_2\otimes\mathbb{1}_2 + a_i\sigma_i\otimes\mathbb{1}_2 + b_j\mathbb{1}_2\otimes\sigma_j + t_{ij}\sigma_i\otimes\sigma_j\right)\,, \tag{2.9b}$$

where the sum convention is used, $i,j \in \{\mathrm{x},\mathrm{y},\mathrm{z}\}$ and $t_{ij} \equiv a_i b_j$. One possible basis for the two-qubit state space is the computational basis $\{|00\rangle, |01\rangle, |10\rangle, |11\rangle\}$. Another possible basis is formed by the four maximally entangled Bell states $\{|\phi^+\rangle, |\psi^+\rangle, |\phi^-\rangle, |\psi^-\rangle\}$. These Bell states can be expressed in the Bloch representation (eq. (2.9)) with $a_i = b_i = 0$, but $t_{ij} = \pm\delta_{ij}$. The coefficients t_{ii} for the four states are summarised in Table 2.1. Maximally entangled here means that the full information the system can carry is encoded in the global correlations and the partial trace over one system leaves the other in the maximally mixed state [24].

Table 2.1: *Coefficients t_{ii} of the Bloch representation of the Bell states. As discussed in section 2.3, the coefficient t_{ii} equals the visibility in the i-basis. Depending on the basis, the visibility of a Bell state is one in case of correlation and minus one in case of anti-correlation. Distinctively, the triplet state ψ^- is anti-correlated in all three bases.*

Bell state	t_{xx}	t_{yy}	t_{zz}
$\|\phi^+\rangle\langle\phi^+\|$	1	-1	1
$\|\psi^+\rangle\langle\psi^+\|$	1	1	-1
$\|\phi^-\rangle\langle\phi^-\|$	-1	1	1
$\|\psi^-\rangle\langle\psi^-\|$	-1	-1	-1

By local operations only any Bell state can be mapped to the others up to global phases. The unilateral Pauli π rotations about an axis k are described by the corresponding Pauli matrix σ_k. Starting from ϕ^+ state, this is demonstrated with the Bell states expressed in the computational basis

$$(\mathbb{1}_2 \otimes \mathbb{1}_2)\,|\phi^+\rangle = \frac{|00\rangle + |11\rangle}{\sqrt{2}} = \quad |\phi^+\rangle\,, \tag{2.10}$$

$$(\mathbb{1}_2 \otimes \sigma_{\mathrm{x}})\,|\phi^+\rangle = \frac{|01\rangle + |10\rangle}{\sqrt{2}} = \quad |\psi^+\rangle\,, \tag{2.11}$$

$$(\mathbb{1}_2 \otimes \sigma_{\mathrm{z}})\,|\phi^+\rangle = \frac{|00\rangle - |11\rangle}{\sqrt{2}} = \quad |\phi^-\rangle\,, \tag{2.12}$$

$$(\mathbb{1}_2 \otimes \mathrm{i}\,\sigma_{\mathrm{y}})\,|\phi^+\rangle = \frac{|10\rangle - |01\rangle}{\sqrt{2}} = -|\psi^-\rangle\,. \tag{2.13}$$

The rotation about the y-axis in equation (2.13) is the same as a π rotation about the x-axis directly followed by a π rotation about the z-axis as $\mathrm{i}\,\sigma_{\mathrm{y}} = \sigma_{\mathrm{z}}\sigma_{\mathrm{x}}$.

2.3 Fidelity and visibility

The fidelity is a measure for the distance between two quantum states ρ and τ

$$F\left(\tau,\rho\right) \equiv \mathrm{tr}\left\{\sqrt{\tau^{\frac{1}{2}}\rho\tau^{\frac{1}{2}}}\right\}^2 . \tag{2.14}$$

It takes the minimal value of 0 if the two states have no common contributions and it is equal to one in case the two states are the same [7]. For pure target states $\tau = \tau^2$, the fidelity simplifies to the overlap of the two states

$$F\left(\tau,\rho\right) = \mathrm{tr}\left\{\tau\rho\right\} . \tag{2.15}$$

For the target state ϕ^+, a two-qubit state ρ in the Bloch representation (eq. (2.9)) and by following the lines of equation (A.1), the fidelity can be expressed as

$$\begin{aligned} F_{\phi^+}(\rho) &= \mathrm{tr}\left\{\frac{1}{4}\left(\mathbb{1}_2 \otimes \mathbb{1}_2 + a_i\sigma_i \otimes \mathbb{1}_2 + b_j\mathbb{1}_2 \otimes \sigma_j + t_{ij}\sigma_i \otimes \sigma_j\right)\right. \\ &\qquad \left.\frac{1}{4}\left(\mathbb{1}_2 \otimes \mathbb{1}_2 + \sigma_\mathrm{x} \otimes \sigma_\mathrm{x} - \sigma_\mathrm{y} \otimes \sigma_\mathrm{y} + \sigma_\mathrm{z} \otimes \sigma_\mathrm{z}\right)\right\} \qquad (2.16a) \\ &= \frac{1}{4}\left(1 + t_\mathrm{xx} - t_\mathrm{yy} + t_\mathrm{zz}\right) . \qquad (2.16b) \end{aligned}$$

As shown in Appendix A.1, the coefficient t_{kk} corresponds to the visibility of the two-qubit state in the k-basis

$$V_{kk}(\rho) = \mathrm{tr}\left\{\rho\left(\sigma_k \otimes \sigma_k\right)\right\} = t_{kk} , \qquad (2.17)$$

with $k \in \{\mathrm{x}, \mathrm{y}, \mathrm{z}\}$. As an example, the visibility of the state ρ in the computational basis is computed as

$$V_\mathrm{zz}(\rho) = \mathrm{tr}\left\{\rho\left(\sigma_\mathrm{z} \otimes \sigma_\mathrm{z}\right)\right\} = \mathrm{tr}\left\{\rho\left(|00\rangle\langle 00| - |01\rangle\langle 01| - |10\rangle\langle 10| + |11\rangle\langle 11|\right)\right\} . \qquad (2.18)$$

Experimentally, the visibility is determined as the contrast between parallel and orthogonal analyser settings $C_\parallel$ and $C_\perp$,

$$V = \frac{C_\parallel - C_\perp}{C_\parallel + C_\perp} , \qquad (2.19)$$

normalised by the total. For correlated states, the visibility is positive, for anti-correlated states the visibility is negative. Bell states, discussed in the previous section, are perfectly correlated, so the visibility in the computational basis takes the extremal values $V_\mathrm{zz} = +1$ for the $\phi^\pm$ states and $V_\mathrm{zz} = -1$ for the $\psi^\pm$ states.

The fidelity with respect to the ϕ^+ can then be computed from the visibilities measured in the three mutually unbiased bases x, y, and z as

$$F_{\phi^+}(\rho) = \frac{1}{4}\left(1 + V_\mathrm{xx}(\rho) - V_\mathrm{yy}(\rho) + V_\mathrm{zz}(\rho)\right) . \qquad (2.20)$$

2.4 Jones formalism

In the Jones formalism the horizontal and vertical polarisation of light are described by the vectors $|\mathrm{H}\rangle = (1,0)^\mathrm{T}$ and $|\mathrm{V}\rangle = (0,1)^\mathrm{T}$. Non-depolarising components are described by 2×2 matrices. A wave plate is a phase retarder that introduces a relative phase between the horizontal and the vertical component

$$W(\xi) \equiv \begin{pmatrix} 1 & 0 \\ 0 & \mathrm{e}^{-i\xi} \end{pmatrix} . \tag{2.21}$$

Special cases of phase retarders are the a quarter-wave plate (QWP) and a half-wave plate (HWP) with $\xi = \pi/2$ and $\xi = \pi$ respectively. The description of a waveplate set at an angle θ is obtained by congruence with the 2-dimensional rotation matrix $R(\theta)$

$$Q_\theta \equiv R(\theta)\, W(\pi/2)\, R(-\theta) \ , \qquad \mathrm{H}_\theta \equiv R(\theta)\, W(\pi)\, R(-\theta) \ , \tag{2.22}$$

with

$$R(\theta) \equiv \begin{pmatrix} \cos\theta & -\sin\theta \\ \sin\theta & \cos\theta \end{pmatrix} . \tag{2.23}$$

A more comprehensive discussion of the formal descriptions of polarisation can be found in [25].

2.5 Single photon counting

The quanta of light are called photons. Each photon carries an energy of $\mathrm{E} = \hbar\omega$, where $\hbar$ is the reduced Planck constant and ω is the frequency of the light. As a consequence of this quantisation, the actual photon number in an optical field fluctuates even if the classical intensity is constant in time [26]. For coherent light of constant intensity such as emitted by a laser, the probability to find n photons in a small time interval is described by the Poisson distribution

$$\mathrm{P}(n;\nu) = \frac{\nu^n}{n!}\mathrm{e}^{-\nu} , \tag{2.24}$$

which is uniquely defined by the mean photon number $\nu = \langle n \rangle$ (see e.g. [27]). The variance σ^2 of the Poisson distribution equals the mean, such that

$$\sigma = \sqrt{\nu} . \tag{2.25}$$

As photons cannot be observed directly, a photon detector converting the light field into an electric current is required for photon counting. If the light is dim, the electric pulses returned by the detector are clearly separated in time and each pulse is associated with a photon incident on the detector. Due to a non-unit quantum efficiency not every photon incident on the detector is detected, but the distribution of pulses returned by the detector is sampled from the photon statistics. With the assumption of a random sampling, also the detector pulses follow Poissonian statistics [27].

The temporal correlation between optical fields at two locations can be analysed by coincidence counting of the pulses returned by two detectors. Each pulse is time tagged. If the difference between a time tag t_1 at one detector and a time tag t_2 at the other detector is smaller than half the defined coincidence window t_{cow},

$$|t_1 - t_2| < \frac{t_{\text{cow}}}{2}\,, \tag{2.26}$$

the two corresponding pulses are declared to be coincident. But not only correlated pairs may lead to a coincidence count. In experiment, loss, non-unit detector efficiency and dark counts lead to coincidence counts of uncorrelated pairs. For local count rates R_1 and R_2 detector one and two respectively, the accidental count rate R_{acc} can be approximated by

$$R_{\text{acc}} \approx R_1 R_2 t_{\text{cow}}\,. \tag{2.27}$$

This approximation is valid for a small number of average counts per coincidence window [28].

3 Generation of entangled photon pairs

The starting point of every experiment working with entangled photons has to be a reliable source of entangled photons. Most commonly nowadays, spontaneous parametric down conversion (SPDC) is used in various configurations. Since the first efficient SPDC source for entangled photon pairs in 1995 [29], the performance was optimised over decades of research and applications [30].

In this section, the process of SPDC is introduced in general. The source configuration as used in the experiment is discussed in detail. In a first step, the generation of entanglement in the polarisation DOF, then the generation of entanglement in the energy-time DOF and the basic working principle of a Franson interferometer are explained. Finally the formal description of independent DOF and applications of simultaneous entanglement in multiple DOF are briefly reviewed.

3.1 Spontaneous parametric down conversion

In an SPDC process a pair of single photons results from a non-linear interaction of a material with a pump photon. When an external electric field is applied to a dielectric material, dipoles contributing to the total internal field are induced. This response of a dielectric material to applied electric fields is described by the polarisation

$$\boldsymbol{P} = \epsilon_0 \left(\boldsymbol{\chi^{(1)}} \boldsymbol{E_1} + \boldsymbol{\chi^{(2)}} \boldsymbol{E_1} \boldsymbol{E_2} + \boldsymbol{\chi^{(3)}} \boldsymbol{E_1} \boldsymbol{E_2} \boldsymbol{E_3} + \dots \right) , \tag{3.1}$$

where ϵ_0 is the vacuum electric permittivity, $\boldsymbol{\chi^{(1)}}$ is the linear susceptibility and $\boldsymbol{\chi^{(2)}}, \boldsymbol{\chi^{(3)}}$ are the second-order and the third-order susceptibility, respectively. While often the proportional description of the polarisation density $P \propto E$ is sufficient, in non-linear materials the higher order susceptibilities become too large to be neglected. More detailed discussions of non-linear optics can be found in various text books, e.g. [31], as well as in specialised books such as [32].

With the second order susceptibility, processes like SPDC are described. SPDC is a three wave mixing process where the photon number is not conserved. A pump photon of frequency ω_p is converted to two photons, one typically called signal with frequency ω_s and the other idler with frequency ω_i (see Fig. 3.1). Even though $\chi^{(2)}$ is non-negligible, it is still small, so the SPDC process is rare and the pump power is much higher compared to the power in the signal and idler modes. In addition, it is spontaneous as it is governed by vacuum fluctuations in the

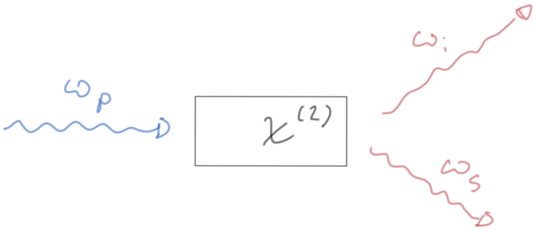

Figure 3.1: *Schematic of three wave mixing in a non-linear medium. A pump photon (ω_p) is converted to a pair of photons, called signal (ω_s) and idler (ω_i).*

lower energy modes. During the down conversion process both, energy and momentum are conserved. The momentum conservation leads to a phase matching condition, that can vary in two aspects. First, the emission can be either non-collinear or collinear with the pump beam. Unlike the non-collinear emission, the collinear emission does not require spatial filtering and so allows for easier alignment and brighter sources as the collection efficiency can be much higher. The second aspect is the polarisation of the emitted photons. Signal and idler photons emitted from type-0 and type-I phase matched sources both have the same polarisation. The polarisation is parallel to the pump photon's polarisation for type-0 and perpendicular to the pump photon's polarisation for type-I phase matching. Whereas photons emitted from type-II sources are of orthogonal polarisation. Phase matching can either be achieved by tuning the angle between the optical axis of the non-linear material and the pump wave vector, or by designing the non-linear material such that the optical axis is flipped periodically. The latter is called quasi phase matching. The flipped domains mutually compensate the spatial walk off and so make longer crystals with a longer interaction length possible. This allows to build brighter sources with narrower bandwidth [30].

3.2 Sagnac configuration

The Sagnac configuration [33, 34] is one of many possible layouts for SPDC sources [30]. A single quasi phase matched non-linear crystal is placed in a polarising Sagnac interferometer and is so pumped from two directions. While the bidirectional pumping does not make use of the full pump power due to the separation into the two directions, it makes compensation for material imperfections of two different crystals superfluous. Moreover, the common path of both pump directions as well as the down converted photons in the collinear case makes this setup especially phase stable. In principle the Sagnac configuration works with all types of phase matching [30]. Here, the focus is on a collinear phase matched type-II crystal as used in the experiment and depicted in Figure 3.2. With a continuous wave pump laser at low power, the probability of multi-pair emission can be neglected and the SPDC photons obey

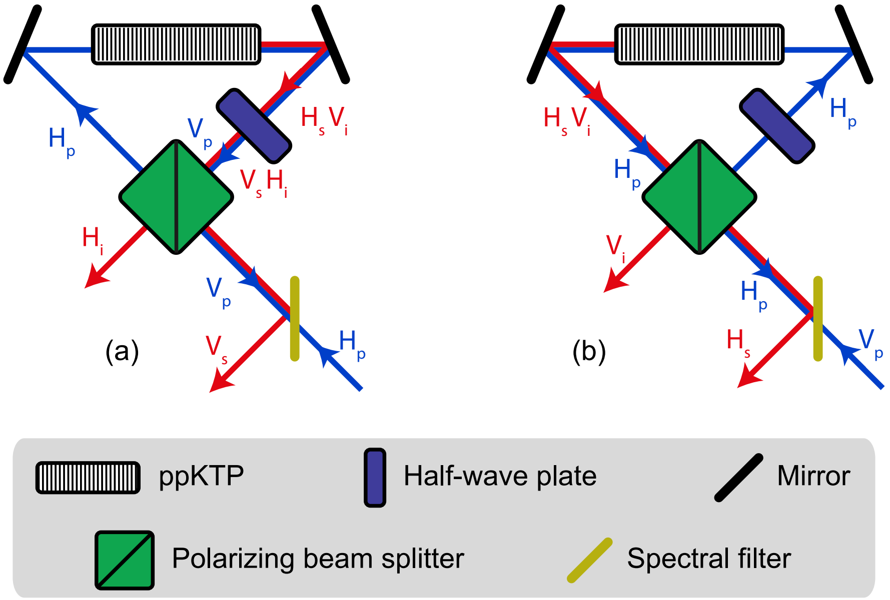

Figure 3.2: *SPDC source with a collinear type-II phase matched periodically polarised Potassium titanyl phosphate (ppKTP) crystal. The pump beam (blue, subscript p) is transmitted by the dichroic mirror. The horizontal component of the pump beam is transmitted by the dual wavelength polarising beam splitter (PBS) and propagates through the Sagnac loop clockwise (a). The polarisation of both, the photon pairs (red, subscript s for signal and i for idler) and the pump beam is flipped by the dual wavelength half-wave plate (HWP) set at an angle of* $\pi/4$*. The idler photons are transmitted, while pump beam and signal photons are reflected by the PBS. At the dichroic mirror, the signal photon is split from the pump beam which is reflected back on itself. In (b) the process for the vertical component of the pump beam is shown. Reflected at the PBS, the pump polarisation is flipped by the HWP so that the pump passes the ppKTP crystal again horizontally polarised. Finally, for this case the signal photons are horizontally polarised and the idler photons are vertically polarised. The superposition of both cases leads to entangled photon pairs as described by equation* (3.2).

Poissonian statistics [35]. The resulting two photon polarisation state

$$|\psi_{\mathrm{SPDC}}\rangle \propto |\mathrm{V_s H_i}\rangle + \mathrm{e}^{\mathrm{i}\,(\phi_\mathrm{p}+\phi_0)}\beta|\mathrm{H_s V_i}\rangle\,, \tag{3.2}$$

can be fully controlled by the phase ϕ_p between the horizontally polarised and the vertically polarised components of the pump laser E_H and E_V as well as their ratio $\beta \propto E_\mathrm{V}/E_\mathrm{H}$. The fixed phase ϕ_0 is determined by material dispersion of the optical components [33].

3.3 Energy-time entanglement and the Franson interferometer

The correlations of photons generated with SPDC sources are not necessarily restricted to polarisation entanglement. Due to energy conservation, entanglement in the energy-time (e-t) degree of freedom (DOF) is always present if the crystal is pumped with a continuous-wave laser [30, 36]. While the emission time of a photon pair is uncertain, the two photons are always emitted simultaneously and the photons created at different times can be coherent to each other. Because time is a continuous variable, the e-t state of an SPDC photon pair is described by the integral

$$|\psi_{\mathrm{SPDC}}\rangle_{\mathrm{e-t}} = \int \mathrm{d}t f\,(t)\,|t\rangle_\mathrm{s}|t\rangle_\mathrm{i}\,, \tag{3.3}$$

where $f\,(t)$ is non-zero over the coherence time of the pump laser τ_{pump} .

In 1989 Franson [37] proposed an experiment to violate a Bell inequality with the e-t DOF. In the subsequent years several experiments demonstrated a violation [38, 39, 40, 41, 42, 43, 44]. In contrast to Franson's original proposal, all the experimental implementations employed SPDC sources for the generation of entangled photons.

The Franson interferometer proposed in [37] consists of two unbalanced Mach-Zehnder (MZ) interferometers A and B as depicted in Figure 3.3. The time delays ΔL_i introduced by the long arms L_i with respect to the short arms S_i should be much larger than the coherence length of the single photons

$$\tau_{\mathrm{sp}} \ll \frac{\Delta L_i}{c} = \frac{L_i - S_i}{c}\,, \tag{3.4}$$

with the speed of light c, such that no interference is observed locally at Alice's or Bob's side. Instead, interference is observed in the coincidence counts if the delays are not larger than the coherence time of the pump laser

$$\frac{\Delta L_i}{c} \ll \tau_{\mathrm{pump}}\,. \tag{3.5}$$

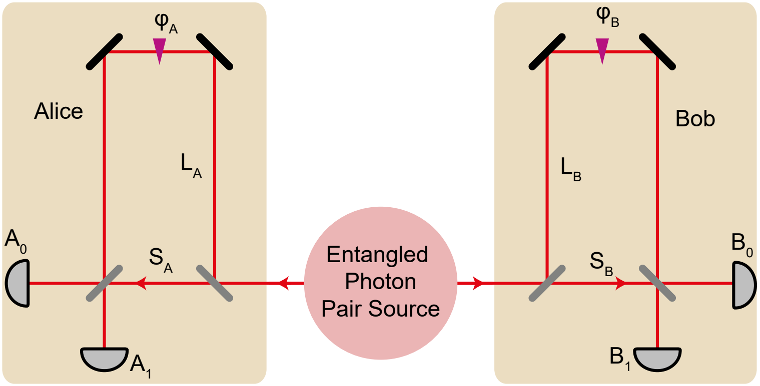

Figure 3.3: *Schematic of a Franson interferometer. One photon of a pair created in the entangled photon pair source enters one arm of the interferometer. Each arm consists of an unbalanced Mach-Zehnder interferometer with one detector per output port. The phases in the long arms,* φ_A *and* φ_B*, are adjustable.*

The latter condition ensures the coherence of the four possible events $\mathrm{S_AS_B}$, $\mathrm{S_AL_B}$, $\mathrm{L_BS_A}$ and $\mathrm{L_AL_B}$. However, as can be seen in the delay histogram sketched in Figure 3.4, the events

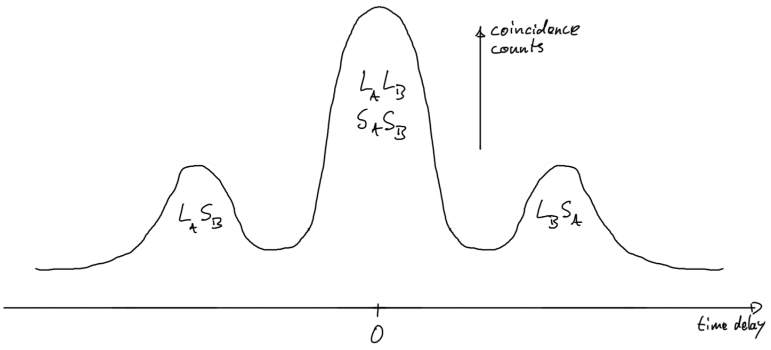

Figure 3.4: *Delay histogram of a Franson interferometer. The central peak at zero time delay contains two interfering contributions. The side peaks form an non interfering background. The units are arbitrary.*

$\mathrm{S_AL_B}$ and $\mathrm{L_AS_B}$ are clearly distinguishable from the others by the temporal delay and so form a non-interfering background. The remaining terms $\mathrm{S_AS_B}$ and $\mathrm{L_AL_B}$ are indistinguishable if the introduced time delays are about the same in both arms

$$\Delta L_\mathrm{A} \approx \Delta L_\mathrm{B}\,. \tag{3.6}$$

When excluding the side peaks, the output state is proportional to a coherent superposition

$$|\psi\rangle \propto |\mathrm{SS}\rangle + \mathrm{e}^{\mathrm{i}\,\phi}|\mathrm{LL}\rangle\,, \tag{3.7}$$

with ϕ equal to the sum of the phases of the single photons

$$\begin{aligned}\phi = \varphi_{\mathrm{A}} + \varphi_{\mathrm{B}} &= \omega_{\mathrm{s}}\frac{\Delta L_{\mathrm{A}}}{c} + \omega_{\mathrm{i}}\frac{\Delta L_{\mathrm{B}}}{c} && \text{(3.8a)}\\ &= \frac{\omega_{\mathrm{s}}+\omega_{\mathrm{i}}}{2c}\left(\Delta L_{\mathrm{A}} + \Delta L_{\mathrm{B}}\right) + \frac{\omega_{\mathrm{s}}-\omega_{\mathrm{i}}}{2c}\left(\Delta L_{\mathrm{A}} - \Delta L_{\mathrm{B}}\right) && \text{(3.8b)}\\ &\approx \frac{\omega_{\mathrm{p}}}{2c}\left(\Delta L_{\mathrm{A}} + \Delta L_{\mathrm{B}}\right) . && \text{(3.8c)}\end{aligned}$$

Then, the coincidence rate with a coincidence window narrowed to the central peak is proportional to

$$\left|1 + \mathrm{e}^{\mathrm{i}\phi}\right|^2 = 2 + 2\cos\left(\frac{\omega_{\mathrm{p}}}{2c}\left(\Delta L_{\mathrm{A}} + \Delta L_{\mathrm{B}}\right)\right) . \tag{3.9}$$

An advanced setup introduced by Strekalov et al [45] employs both, the polarisation entanglement and the e-t entanglement of photon pairs created with an SPDC source to circumvent the post-selection on the central peak. The experimental setup was varied only slightly by replacing the four BS with PBS.

3.4 Hyperentanglement

As mentioned in the previous sections, quantum systems are not restricted to entanglement in one DOF only. The state of a system that is entangled in multiple DOF is called hyperentangled [36, 46]. Formally, the states of different DOF are treated exactly like states of different copies of a quantum systems like multiple qubits. If they are independent of each other, they can be expressed as product state. For the simplest case of two DOF this is

$$\rho = \rho_{\mathrm{DOF1}} \otimes \rho_{\mathrm{DOF2}} . \tag{3.10}$$

Hyperentanglement has been used to improve existing quantum information processing protocols. Following a proposal by Kwiat and Weinfurter [47], several experimental implementations demonstrated an improvement of the Bell state analysis [48, 49, 50]. The Bell state analysis is a building block not only of dense coding, that has the goal to increase the channel capacity [51], but also of quantum teleportation [10, 11] and entanglement swapping [13]. Further, the noise resilience is not only increased since hyperentangled states live in a larger Hilbert space, but also due to the fact, that the DOF vary in their sensitivity to different noise sources. This has been used to improve entanglement distribution [52, 53].

4 Entanglement distillation

In this section, entanglement distillation is motivated and historical aspects are given. The entanglement distillation scheme on which the experiment is based as well as earlier photonic entanglement distillation experiments are reviewed in detail.

4.1 Introduction to entanglement distillation

Quantum entanglement shared over long distances is indispensable for many quantum communication tasks. Because entanglement cannot be produced by local operations and classical communication of remote parties, it is first produced at one location and then distributed to the corresponding communication parties via quantum channels. Due to interaction with the environment, dissipation and decoherence inevitably reduce the purity and so the entanglement of the shared quantum states.

If instead of just one copy of a certain maximally entangled state, multiple copies are distributed, the originally sent state can be reconstructed by local operations and classical communication. Entanglement distillation protocols increase the entanglement of an ensemble of quantum states at the expense of the number of copies [8, 14]. By joint but local operations, entangling actions and measurements as well as classical two-way communication for postselection, $M < N$ states of close to maximal entanglement can be distilled from N not too impure input states. Aside from the reachable fidelity, the yield $Y = M/N$ as well as the distillation basin, that is the region of useful positive gain, are measures for the performance of an entanglement distillation protocol.

The first entanglement distillation protocols were proposed in 1996. Bennett et al (BBPSSW) [8] introduced their protocol in the context of quantum teleportation and the simulation of a noiseless quantum channel. The scheme presented by Deutsch et al (DEJMPS) [14] is very similar to the BBPSSW scheme but was originally discussed in the context of quantum key distribution. There is no consensus within the scientific community on the terminology. Both the term entanglement distillation and the term entanglement purification date back to 1996 [8, 14, 15]. Here the term entanglement distillation is used as it is considered more descriptive and avoids possible confusion due to the different use of the term purification by theorists [7]. Other terms such as entanglement concentration [16] and filtering [17] that appear in this context denote fundamentally different schemes. Protocols known as filtering act on one copy at a time. By non-unitary, local operations unwanted contributions are filtered out [54, 55, 56]. Asymptotic protocols such as hashing or breeding, on the contrary, act on a large number of input states in a single step [8, 57]. The number and position of errors in the ensemble is identified and can be corrected subsequently. While they offer the benefit of a nonzero yield, a low tolerance for noisy operations and a required high input fidelity makes them not feasible in real applications. A third group of entanglement distillation protocols contains the two aforementioned proposals by BBPSSW and DEJMPS [8, 14]. Recurrence protocols act on a fixed number, mostly two identical copies of qubit pairs at a time. The output of a successful distillation step is used as input for the next distillation step. With each iteration the attractive fixpoint of unit fidelity is approached. The number copies required grows exponentially with the number of distillation steps and the yield for unit fidelity is zero.

4.2 BBPSSW entanglement distillation scheme

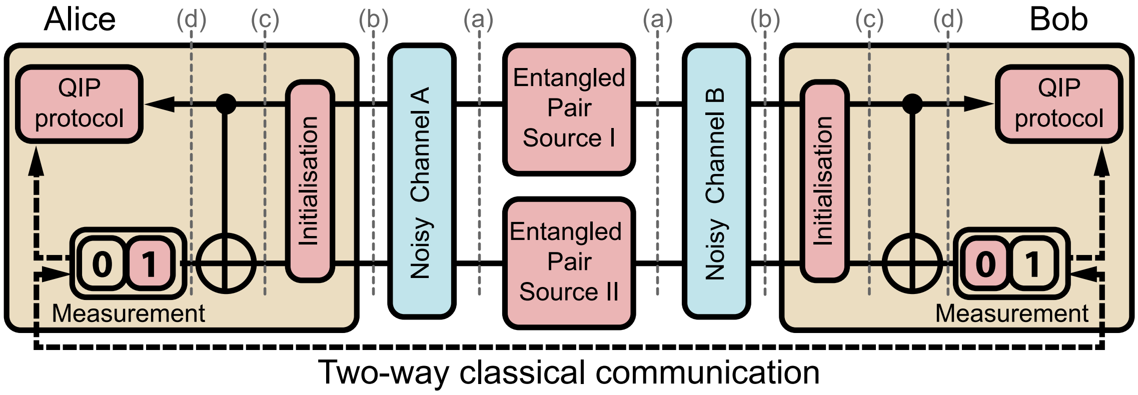

Figure 4.1: *Circuit diagram of the entanglement distillation scheme as introduced by BBPSSW [8]. This scheme forms the basis for the single-copy entanglement distillation protocol experiment performed during this masters project. The grey vertical dashed lines indicate stops used to explain the scheme in the text.*

Here, the recurrence protocol as introduced by BBPSSW [8] will be discussed in more depth, since this is the basis for the experiment performed. A single distillation step is illustrated in a circuit diagram in Figure 4.1. Two singlet states ψ^- are produced by the sources I and II. At the position (a) in the diagram, the state of both entangled pairs is a pure state. One qubit of each pair is sent to one party, Alice or Bob. Due to the effect of noisy channels, these pure states evolve to mixed states (b) during transmission. While the qubits sent to Alice may experience a different noisy channel than those sent to Bob, both qubits sent to one party experience the same noisy channel such that the pairs I and II are in the same mixed state. The incoming mixed states are initialised by bilateral and unilateral rotations, which turn unknown noise into white noise and prepare the state for the actual distillation. At this point, the initialisation step is only very briefly reviewed. A more detailed discussion of this procedure can be found in references [8, 9].

The first part of the initialisation step is the application of the same random rotations on both qubits of a pair. These bilateral rotations leave the singlet state ψ^- invariant and transform the triplet states ψ^+, ϕ^+ and ϕ^- into each other. The result is a Werner state [22], that is a singlet state with admixed white noise, having the same fidelity with respect to the singlet state as the input state. Consequently, all input states with the same singlet state fidelity end up in the same Werner state.

In the second part of the initialisation step, the Werner state is prepared for the subsequent distillation process. By a unilateral π rotation about the y-axis, the dominant contribution of the singlet state is transformed to a contribution of the ϕ^+ state (c). As introduced in section 2.2, a π rotation about the y-axis is described by the Pauli matrix σ_{y}. The noise remains unchanged, such that a Werner state of fidelity F is transformed like

$$(\mathbb{1}_2 \otimes \sigma_{\mathrm{y}})\,(2F-1)\,|\psi^-\rangle\langle\psi^-| + (1-F)\,\mathbb{1} = (2F-1)\,|\phi^+\rangle\langle\phi^+| + (1-F)\,\mathbb{1}\,. \tag{4.1}$$

This initialisation is crucial for recurring distillation steps and ensures the universality of the BBPSSW scheme. For the following steps it is sufficient to discuss the case of a Werner like state.

At the core of the scheme is the bilateral controlled NOT (bCNOT) gate. The qubits of pair I are used as control and the qubits of pair II are used as target. The bCNOT itself does not change the fidelity of the ensemble but permutes the entries of the Bell diagonal matrix (d) as shown in Table A.1 in appendix A.2. Only in combination with a post-selection a subset of increased Bell state fidelity can be selected. For the post-selection, the qubits of the target pair are measured in the computational basis by both parties and the results are compared via classical two-way communication. If the measurement outcomes are the same, the control pair is kept, otherwise it is discarded. The measurements of the target pair consume half of the input pairs a priori and thereby limit the yield from above to one half. The yield is further lowered by discarding control pairs depending on the input state.

The performance of the scheme is illustrated in Figure 4.2. For input pairs of equal input fidelities (a) there are three distinct regions to discuss. Between 0.25 and 0.5 input fidelity the gain is negative, so in this region the scheme fails. The positive gain for input fidelitites below 0.25 is not interesting, as the maximal output fidelity does not exceed the fidelity of the maximally mixed state. A positive, useful gain can be obtained for input fidelities larger than one half. The fixpoint of that region is at unit fidelity. But due to the low success probability per step and the number of required distillation steps, the global yield for unit fidelity goes to zero. As soon as the input fidelitites of the two pairs involved in one purification step are not the same (b), the gain with respect to the maximal input fidelity, that is depicted in Figure 4.2 (b) drops compared to the BBPSSW case of equal input fidelities. The region of positive gain is also called distillation basin.

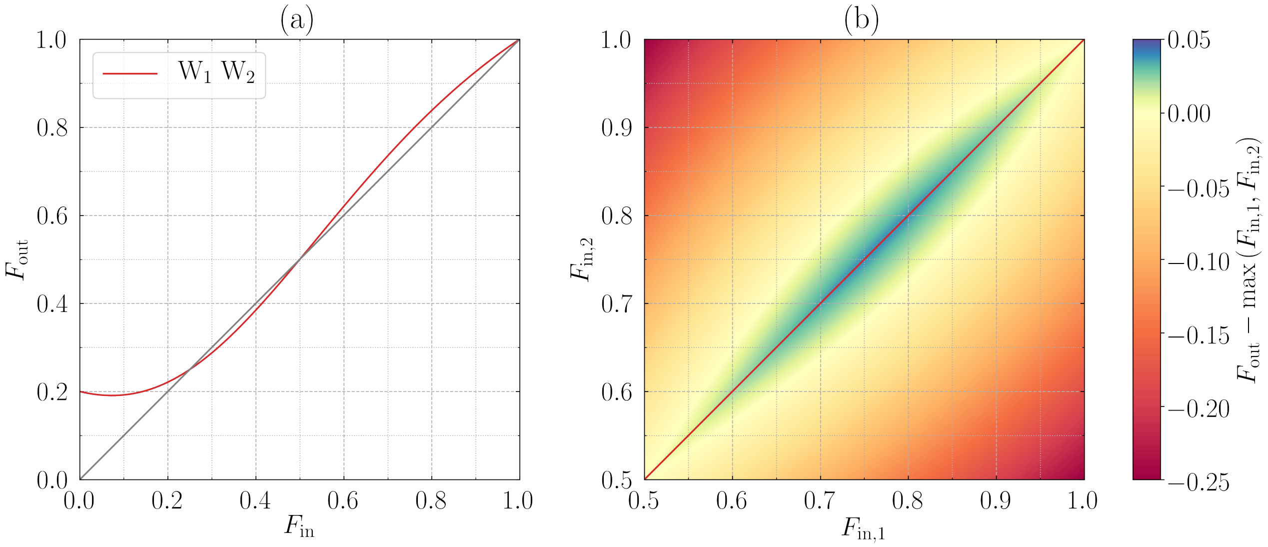

Figure 4.2: *The gain in fidelity for a Werner state in both input qubit pairs. On the left (a) the output fidelity is plotted as a function of the input fidelity (red line). The diagonal indicates zero gain. The only useful gain can be obtained for input fidelities larger than one half. This region is depicted in the frame on the right hand side (b). The input fidelity of pair I is shown on the* x*-axis and the fidelity of pair II is shown on the* y*-axis. The colour indicates the gain with respect to the maximal input fidelity. The cut along the diagonal corresponds to the case depicted on the left (a). The maximum gain is reached for equal input fidelities and the gain becomes negative for large differences in the input fidelities.*

4.3 Photonic entanglement distillation

Photons are good qubit carriers for quantum communication tasks. They travel at a high speed and interact little with the environment. It is therefore desirable to implement photonic entanglement distillation protocols. The Bennet scheme discussed in the previous section relies on two controlled NOT (CNOT) gates. Unfortunately it is especially challenging to implement a photonic CNOT gate that acts on qubits carried by two different photons with a sufficiently low error rate [58, 59, 60, 61].

Based on the BBPSSW scheme Pan et al [62] proposed an experiment for a single distillation step without twirling with two polarisation entangled photon pairs and passive linear optics. They analyse that a CNOT gate followed by a measurement of the target bit corresponds to a full parity measurement. Depending on the state of the control qubit, the CNOT gate flips the logical state (0 or 1) of the target qubit. If the target qubit is found to be in the logical state 0 after the action of the CNOT gate, both qubits had the same state before, i.e. the input states were of even parity. If the target qubit is found to be in the logical state 1 after the action of the CNOT gate, the input states were of odd parity. They continue by pointing out, that at least a test for even parity of two independent polarisation qubits can be performed by overlapping two photons at a PBS followed by coincidence measurement. For a successful distillation step, the communication parties have to prove even parity by four-fold coincidences.

Additionally, one pair has to be measured in the diagonal basis. Depending on the outcome, a phase correction is required to obtain a ϕ^+ state. The fidelity reached with this protocol is the same as in the BBPSSW scheme. But, due to the demanding post-selection criterion it has only half the success probability for each step and so a much lower yield. Experimentally, the overlap at the PBS is challenging, especially with two independent sources as sketched in this proposal by Pan et al [62].

This problem has been addressed in a proposal by Simon et al [63]. They suggest a single non-linear crystal passed twice by a pulsed pump. By fixing the phase between the two passages of the pump laser, not only polarisation entanglement, but also path entanglement is generated independently. With such an hyperentangled state, a PBS can actually act as CNOT with the polarisation DOF as control and the path DOF as target. The action of the PBS as CNOT is discussed in more detail in section 5. For the post-selection, no polarisation qubits are consumed. But instead the path DOF is consumed by the choice of the combination of output port. Regarding the success probability of polarisation qubits, this protocol outperforms also the BBPSSW scheme by employing hyperentanglement. A drawback of establishing the spatial entanglement at the source is the required phase stability on the scale of the wavelength for the possible paths the photons can take.

Experimentally, photonic entanglement distillation based on the BBPSSW scheme has been shown by Pan et al [64]. The setup is apparently influenced by the improved proposal [63], but the post-selection still relies on four fold coincidences following [62]. They were able to meet the high demands on stability and successfully distilled entanglement from a state including a bit flip error. With a similar setup Walther et al [65] demonstrated that with entanglement distillation an ensemble not violating a Bell inequality can be lifted above the threshold to violate a Bell inequality.

5 Experimental single-copy entanglement distillation

In this section, the authors contributions to the experiment performed during this masters project will be presented in detail. To begin with, the basic working principle of the single-copy distillation scheme is presented in section 5.1. Essential differences to previous schemes are pointed out. The generation of noise, theoretically and experimentally, in both DOF, polarisation and energy-time, is discussed in section 5.2. In section 5.3 the mathematical model developed specifically for this experiment is introduced. This model is used to simulate the experiment and illustrate the performance of the scheme by comprehensible examples. Experimental imperfections and adaptions of the model to close the gap between theory and experiment are discussed. The setup of the experimental implementation and the different configurations for the measurements of the fidelities are described in sections 5.4 and 5.5.

5.1 Principle of the single-copy entanglement distillation scheme

The entanglement distillation protocol demonstrated here uses passive linear optics and photons entangled in both, the polarisation DOF, and the energy-time (e-t) DOF. Similarly to the proposal by Simon and Pan [63], only one photon pair is used per distillation step. But rather than the proposed spatial DOF, the e-t DOF is used as additional resource to improve the entanglement in the polarisation DOF. The e-t DOF offers the benefit, that, in contrast to the spatial DOF, no phase stability is required for distribution.

The circuit diagram of this single-copy distillation scheme as shown in Figure 5.1 could lead to the misunderstanding that the two DOF are split up spatially or that more than one pair of photons is involved per step. Neither is the case. The diagram should rather illustrate that the qubits encoded in independent DOF of one photon pair can be treated the same way as qubits encoded in the same DOF of two pairs as depicted in Figure 4.1. But unlike two-copy entanglement distillation [64], where both qubit pairs are encoded in the same DOF, the yield can be doubled in single-copy entanglement distillation. Measuring the auxiliary DOF for post-selection does not reduce the yield in the DOF to be distilled. This allows for a yield of up to 1 to be achieved.

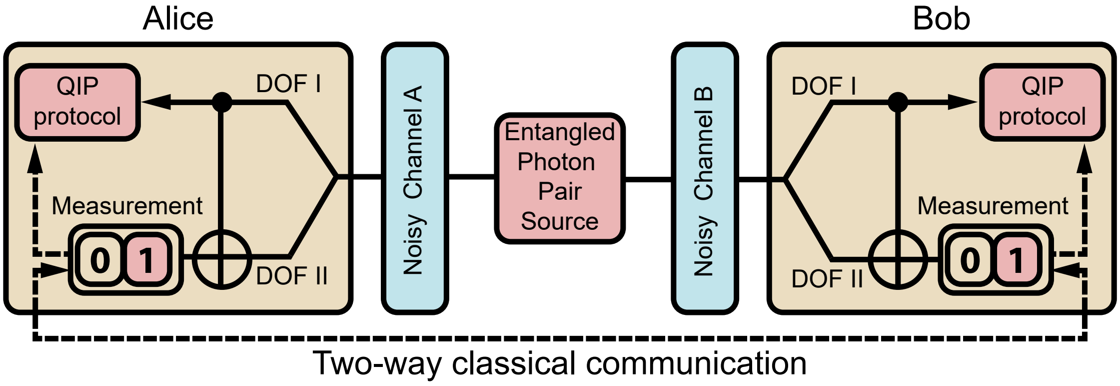

Figure 5.1: *Circuit diagrams of single-copy entanglement distillation. This diagram should stress the similarities and differences with the BBPSSW scheme shown in Figure 4.1. Both schemes have a bilateral CNOT at the core. The initialisation is omitted here, as only one step is conducted. In contrast to the BBPSSW scheme, here only one photon pair entangled in two DOF is created by a single source and only two quantum channels are needed for distribution. The two DOF have a very different susceptibility to the action of the noisy channels. After application of the bCNOT, in both schemes, the source qubit pair is post-selected according to the measurement result of the target qubit pair.*

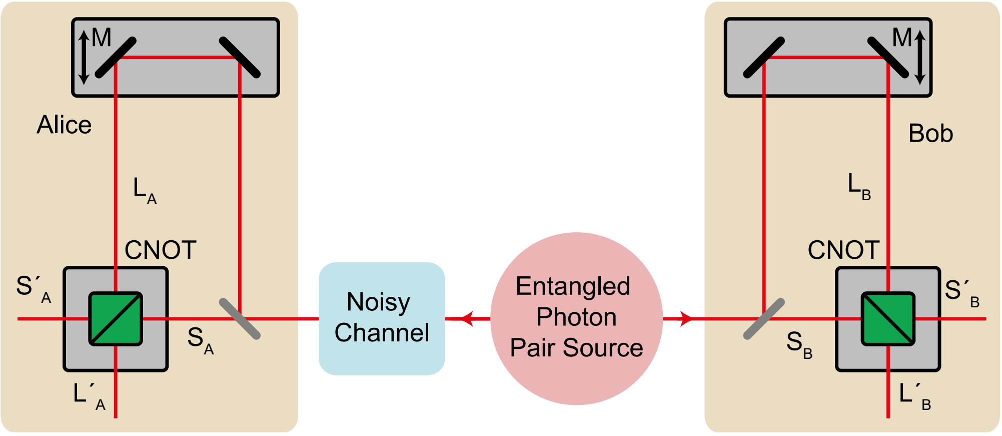

Figure 5.2: *Conceptual schematic of the single-copy entanglement distillation scheme. Photon pairs entangled in both, polarisation and energy-time, are generated at the source. With a controlled noisy channel, entanglement can be degraded on purpose before it is distilled again. The PBS in the Franson type interferometer act as bCNOT. By coincidence measurement in the output channels* S'_A *and* S'_B *as well as* L'_A *and* L'_B *post-selection on the* $\phi^\pm$ *Bell states in the e-t DOF is realised. The aim of the single-copy entanglement distillation scheme is to increase the Bell state fidelity in the polarisation DOF at the expense of entanglement in the e-t DOF. The motorised (M) stages are used to adjust to high Franson visibility and to control the phase in the long paths.*

Experimentally, the single-copy entanglement distillation scheme for the polarisation and the e-t DOF is implemented with a Franson type interferometer as shown in Figure 5.2. The especially noise resilient e-t DOF is projected onto a two dimensional subspace of delays $\{\mathrm{SS}, \mathrm{SL}, \mathrm{LS}, \mathrm{LL}\}$. Because the temporal delays can be directly associated with the length of the different spatial paths, the labels long L and short S are used and the DOF is occasionally called path DOF. In the modified Franson interferometer as it is shown in Figure 5.2 the exit BS in each arm of the Franson interferometer, as introduced in section 3.3, is replaced with a PBS. These PBS act locally as CNOT gates on the polarisation and the path DOF of one and the same photon. Here, the polarisation DOF acts as control and the path DOF as target. Horizontally polarised photons are transmitted, so the path DOF is not affected. Vertical photons are reflected, so the path DOF is flipped.

Table 5.1: *Truth table of a CNOT gate on the left compared with the input and output of a PBS on the right. The first label is the control and the second label is the target. The labels for the spatial modes are as used in Figure 5.2.*

logic				PBS			
before		after		before		after	
0	0	0	0	H	S	H	S′
0	1	0	1	H	L	H	L′
1	0	1	1	V	S	V	L′
1	1	1	0	V	L	V	S′

In Table 5.1 the analogy between a CNOT acting on logical states 0 and 1 and a PBS is shown in a truth table. Horizontally polarised light (H) as well as the short path before (S) and after (S′) the PBS can be associated with the logical state 0. Vertically polarised light (V) as well as the long path before (L) and after (L′) the PBS can be associated with the logical state 1. The action of the bCNOT on the Bell basis is discussed in appendix A.2. It is remarkable that all combinations of control and target states are permuted but only the combination of ϕ^+ in both DOF is left invariant. This property distinguishes the ϕ^+ state from the other Bell states and makes it the natural target state for entanglement distillation.

The measurement of the auxiliary e-t DOF for post-selection is performed implicitly by the choice of output ports of the interferometer.

5.2 Producing the noise

For the experiment, it is crucial to be in control over the input states. Only with an accurate control it is possible to test various contributions of distinct noise models.

The noisy channel as sketched in Figure 5.2 acts on the transmitted photons, but does not have the same effect on the two DOF, polarisation and energy-time. Since both independent DOF have a very different susceptibility to environmental influences, they can and must be manipulated separately. It is sufficient to have a noisy channel in the arm of one party only as all Bell states can be transformed into each other locally as demonstrated in eqns. (2.10) to (2.13).

5.2.1 Noise in polarisation

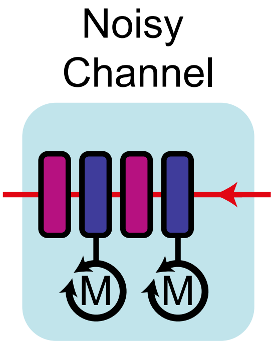

Figure 5.3: *Schematic of the noisy polarisation channel. With this set of two HWP and two QWP it is possible to reach every state on the Bloch sphere. The HWP are motorised (M) such that they can be rotated quickly and precisely.*

The polarisation DOF of the input state is manipulated in a controlled fashion with a combination of four alternating QWP and HWP as depicted in Figure 5.3. In the following, this combination will be called HQHQ channel or simply noisy channel.

To understand the action of the noisy channel and how it is used to create mixed states in polarisation, it will be analysed locally first. So the input state is a single polarisation qubit. The effect on two-qubit states will be discussed thereafter.

Noisy polarisation channel acting on one qubit

Assume the second HWP, sandwiched by the QWP, to be set to ϑ and the other three wave plates set to 0°. Then, a horizontally polarised input, expressed in the Jones formalism (cf. section 2.4), is transformed as

$$Q_0 H_\vartheta Q_0 H_0 |\mathrm{H}\rangle = \cos(2\vartheta)\,|\mathrm{H}\rangle - \mathrm{i}\sin(2\vartheta)\,|\mathrm{V}\rangle\,. \tag{5.1}$$

Because the action of the HQHQ channel can be described by a unitary transformation, the pure input state is transformed to a pure output state. By setting the second HWP to $-\vartheta$, a horizontally polarised input is transformed to $\cos(2\vartheta)\,|\mathrm{H}\rangle + \mathrm{i}\sin(2\vartheta)\,|\mathrm{V}\rangle$, which is also a pure state. If half of the time the channel is set to $+\vartheta$ and the other half it is set to $-\vartheta$, the ensemble average is a mixed state depicted in Figure 5.4 in a cut of the Bloch ball. The convex combination of the two pure states with balanced contributions is located on the z-axis and

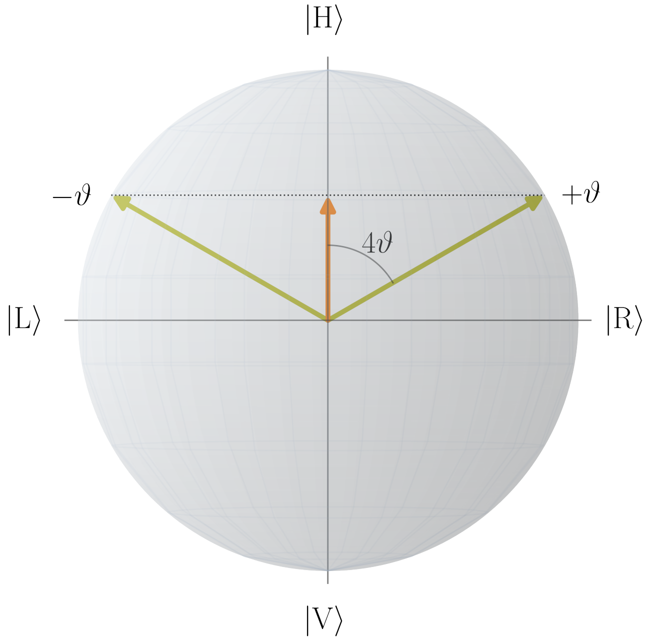

Figure 5.4: *Cut of the Bloch ball spanned by* H/V *and* R/L *basis. The noisy polarisation channel in bit flip configurations rotates input states about the* x-axis (D/A-*basis), that points into the drawing plane. The channel set at* ϑ *corresponds to a rotation by* 4ϑ *on the Bloch sphere. The resulting pure states for channel settings* $\pm\vartheta$ *are marked with green arrows pointing to the surface of the sphere. The equal mixture of both cases is marked by the orange arrow on the* z-axis (H/V-*basis) pointing to the inside of the ball.*

so can be represented by a diagonal matrix in the H/V basis

$$\frac{\rho_{+\vartheta}+\rho_{-\vartheta}}{2} = \frac{1}{2}Q_0 H_\vartheta Q_0 H_0 |\mathrm{H}\rangle\langle\mathrm{H}| \left(Q_0 H_\vartheta Q_0 H_0\right)^\dagger + \frac{1}{2}Q_0 H_{-\vartheta} Q_0 H_0 |\mathrm{H}\rangle\langle\mathrm{H}| \left(Q_0 H_{-\vartheta} Q_0 H_0\right)^\dagger \tag{5.2a}$$

$$= \cos^2(2\vartheta)\,|\mathrm{H}\rangle\langle\mathrm{H}| + \sin^2(2\vartheta)\,|\mathrm{V}\rangle\langle\mathrm{V}|\,, \tag{5.2b}$$

and the fidelity with respect to the horizontally polarised state is $F_\mathrm{H}(\vartheta) = \cos^2(2\vartheta)$.

The performance of the noisy channel has been measured with the alignment laser (810 nm) and a polarimeter, which can track the polarisation of coherent light. The results as well as the theoretical prediction for the rotation about the x-axis are shown in Figure 5.5.

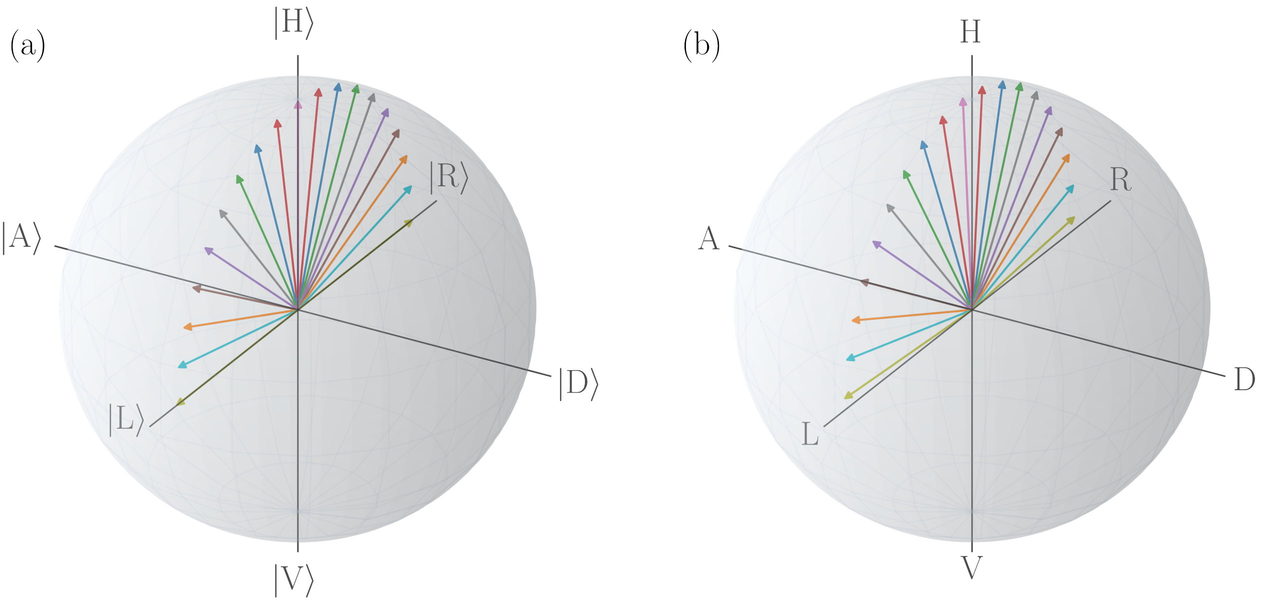

Figure 5.5: *Bloch sphere representation of the action of the polarisation noisy channel in theory (a) and in experiment (b). The setting for the bit flip rotates the state about the* x*-axis* (D/A*-basis). Arrows of the same colour represent the Bell state vectors of the polarisation obtained for waveplate settings at angles of the same magnitude, which was scanned in steps of* 2.5°*. The experimental data was taken with a polarimeter measuring the polarisation state of the red alignment laser. Strictly speaking, (b) does not show a Bloch sphere, but a Poincare sphere in the typical Bloch sphere orientation. The comparison of experiment (b) and theory (a) highlights the excellent performance of the noisy channel.*

Similarly rotations about the other axes can be performed as shown in Figure 5.6.

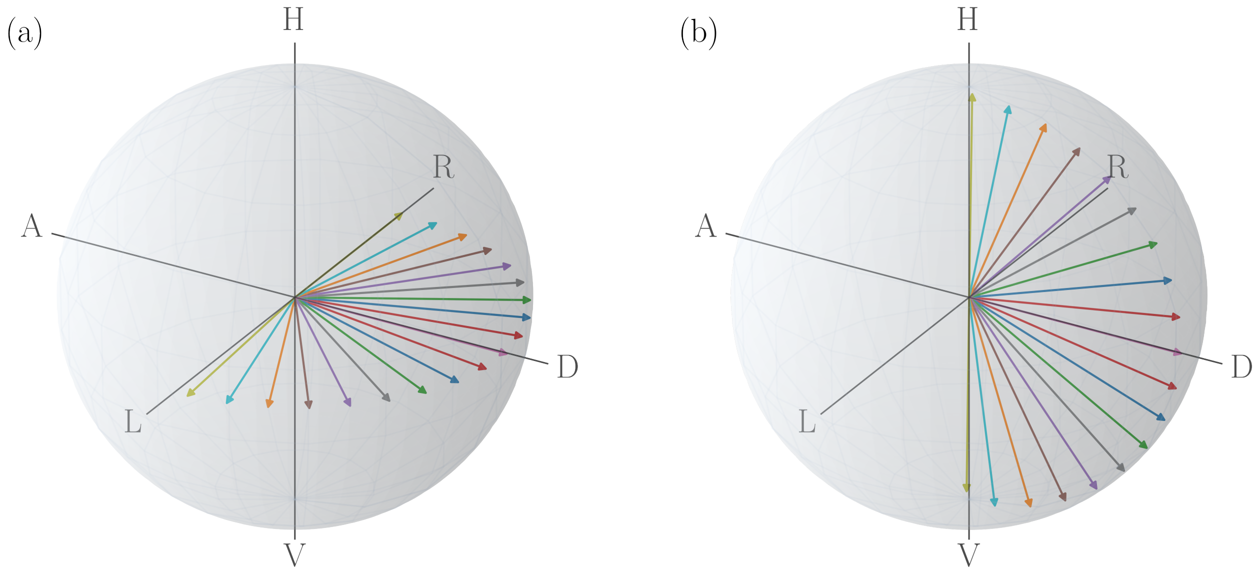

Figure 5.6: *Bloch sphere representation of the action of the polarisation noisy channel. With different settings of the noisy channel it is possible to rotate the polarisation (a) about the* z-axis *(*H/V*-basis), (b) about the* y-axis *(*R/L*)-basis. The arrows indicate the polarisation of the* 810 nm *alignment laser after the noisy channel measured with a polarimeter. The angle set at the noisy channel has been scanned in steps of* $2.5°$ *from* $\pm 0°$ *to* $\pm 22.5°$.

Noisy polarisation channel acting on two qubits

Returning to two-qubits states, these rotations on one qubit can map all Bell states to each other as discussed in section 2.2. With the HQHQ channel set at zero, the state prior to the distillation setup should be the ϕ^+ state. Since the HQHQ channel in the experimental implementation is not designed to be removed and there is no neutral setting in the sense that could be described by an identity matrix, the setting for the channel alignment was chosen with all wave plates set to 0. In total, the HQHQ channel then acts like a $1,5$-wave plate, which can be treated as HWP. This de facto HWP has to be treated as part of the channel that is always present and the angles have to be chosen accordingly as discussed in appendix A.3. As a result the input state of the noisy channel is a ϕ^- state that is transformed as

$$\rho_{\mathrm{QHQH}}\left(\alpha,\beta,\gamma,\delta\right) \equiv \left(Q_\delta H_\gamma Q_\beta H_\alpha \otimes \mathbb{1}_2\right)|\phi^-\rangle\langle\phi^-|\left(H_\alpha^\dagger Q_\beta^\dagger H_\gamma^\dagger Q_\delta^\dagger \otimes \mathbb{1}_2\right) . \tag{5.3}$$

With the similar configuration as for the single qubit case discussed before and the same procedure of averaging over the $\pm\vartheta$ settings, a mixed state diagonal in the Bell basis

$$\frac{1}{2}\rho_{\mathrm{QHQH}}\left(\vartheta,0,0,0\right) + \frac{1}{2}\rho_{\mathrm{QHQH}}\left(-\vartheta,0,0,0\right) = \cos^2\left(2\vartheta\right)|\phi^+\rangle\langle\phi^+| + \sin^2\left(2\vartheta\right)|\psi^+\rangle\langle\psi^+| , \tag{5.4}$$

with adjustable contributions of the ϕ^+ and the ψ^+ states is obtained. The fidelity of this state with respect to the ϕ^+ state is

$$F_{\phi^+}(\vartheta) = \cos^2(2\vartheta) \ . \tag{5.5}$$

Unless specifically stated otherwise, from here on all fidelities should be understood with respect to the ϕ^+ state. Accordingly, phase and combined bit and phase flip contributions can be produced by suitable settings summarised in Table 5.2.

Table 5.2: *The angles to set the quarter-wave plates* (Q) *and the half-wave plates (*H*) at to produce mixed states in polarisation with a well defined error. The wave plate acting on the incoming photons first stands right in the table. Given an input state ϕ^-, a bit flip (ψ^+), a phase flip (ϕ^-) as well as a bit-phase flip error (ψ^-) with respect to the ϕ^+ state can be produced with the noisy channel settings specified in the table. To obtain the mixed state given in the first column, the two settings per row must be chosen with equal probability per integration time.*

output state	Q	H	Q	H
$F(\vartheta)\,\lvert\phi^+\rangle\langle\phi^+\rvert + (1-F(\vartheta))\,\lvert\psi^+\rangle\langle\psi^+\rvert$	0	$\pm\vartheta$	0	0
$F(\vartheta)\,\lvert\phi^+\rangle\langle\phi^+\rvert + (1-F(\vartheta))\,\lvert\phi^-\rangle\langle\phi^-\rvert$	$\pi/4$	$\pm(\pi/4-\vartheta)$	$\pi/4$	0
$F(\vartheta)\,\lvert\phi^+\rangle\langle\phi^+\rvert + (1-F(\vartheta))\,\lvert\psi^-\rangle\langle\psi^-\rvert$	0	0	0	$\pm\vartheta$

5.2.2 Noise in energy-time

The energy-time DOF is more robust than the polarisation DOF. What is good for real quantum communication applications, is a challenge for a proof of principle experiment in the lab. An early idea for introducing a bit flip error in e-t by hardware employed an additional Franson interferometer. The idea was discarded as the stabilisation of four imbalanced Mach-Zehnder interferometers would be experimentally challenging. More details on this idea can be found in appendix A.4. Finally, the noise was produced by widening the coincidence window in the postprocessing. Recalling the Franson interferometer discussed in section 3.3, there are two coherent contributions LL and SS to the peak around zero time difference which allow to see interference. The two distinguishable terms SL and LS, that form a non-interfering background, are usually excluded by post-selection. Assuming the Franson interferometer is adjusted to constructive interference in the ϕ^+ state and the side peaks are of equal magnitude, then widening the coincidence window results in the mixed state

$$\rho_{\mathrm{e-t}} = F\left(\lvert \mathrm{SS}\rangle + \lvert \mathrm{LL}\rangle\right)\left(\langle \mathrm{SS}\rvert + \langle \mathrm{LL}\rvert\right) + \frac{1-F}{2}\left(\lvert \mathrm{LS}\rangle\langle \mathrm{LS}\rvert + \lvert \mathrm{SL}\rangle\langle \mathrm{SL}\rvert\right) \ . \tag{5.6}$$

This incoherent admixture is actually the same as a mixed state with equal ψ^+ and ψ^- contributions

$$\begin{aligned}
|\psi^+\rangle_{\mathrm{e-t}}\langle\psi^+| + |\psi^-\rangle_{\mathrm{e-t}}\langle\psi^-| &= \frac{1}{2}\left(|\mathrm{SL}\rangle + |\mathrm{LS}\rangle\right)\left(\langle\mathrm{SL}| + \langle\mathrm{LS}|\right) \\
&\quad + \frac{1}{2}\left(|\mathrm{SL}\rangle - |\mathrm{LS}\rangle\right)\left(\langle\mathrm{SL}| - \langle\mathrm{LS}|\right) \qquad (5.7a)\\
&= \frac{1}{2}\left(|\mathrm{SL}\rangle\langle\mathrm{SL}| + |\mathrm{SL}\rangle\langle\mathrm{LS}| + |\mathrm{LS}\rangle\langle\mathrm{SL}| + |\mathrm{LS}\rangle\langle\mathrm{LS}|\right) \\
&\quad + \frac{1}{2}\left(|\mathrm{SL}\rangle\langle\mathrm{SL}| - |\mathrm{SL}\rangle\langle\mathrm{LS}| - |\mathrm{LS}\rangle\langle\mathrm{SL}| + |\mathrm{LS}\rangle\langle\mathrm{LS}|\right) \qquad (5.7b)\\
&= |\mathrm{LS}\rangle\langle\mathrm{LS}| + |\mathrm{SL}\rangle\langle\mathrm{SL}| \,. \qquad (5.7c)
\end{aligned}$$

5.3 Simulation of single-copy entanglement distillation

To get an idea of the capability of the protocol, it is useful to simulate the experiment. During this masters project a mathematical model was developed specifically for this experiment. This model is introduced in section 5.3.1 and is used to illustrate the performance of the scheme with comprehensible examples in section 5.3.2. An adapted model accounting for experimental imperfections is discussed in section 5.3.3.

5.3.1 Mathematical model

Following equation (3.10), the state right before the two PBS is described by independent states in both DOF, energy-time and polarisation

$$\rho_{\mathrm{init}} = \rho_{\mathrm{pol,init}} \otimes \rho_{\mathrm{e-t,init}} \,. \qquad (5.8)$$

This description excludes global noise in the sense of noise that can only be described in the common Hilbert space.

The PBS act as bCNOT and permute the entries of the density matrices. In the model this is described by a unitary matrix $\mathrm{U}_{\mathrm{bCNOT}}$ discussed in appendix A.2. While the bCNOT does not change the fidelity of the ensemble, the post-selection does. The criterion of coincidences in parallel output ports is described by the projection on the $\phi^\pm$ states in the e-t DOF

$$P_{\phi^\pm} = \mathbb{1}_{\mathrm{pol}} \otimes \left[|\phi^+\rangle_{\mathrm{e-t}}\langle\phi^+| + |\phi^-\rangle_{\mathrm{e-t}}\langle\phi^-|\right] \,, \qquad (5.9)$$

such that the state after purification can be described as

$$\rho_{\mathrm{post}} = \frac{\mathrm{P}_{\phi^\pm}\rho_{\mathrm{bCNOT}}\mathrm{P}_{\phi^\pm}}{\mathrm{tr}\left\{\mathrm{P}_{\phi^\pm}\rho_{\mathrm{bCNOT}}\right\}}\,, \tag{5.10}$$

with the state

$$\rho_{\mathrm{bCNOT}} = \mathrm{U}_{\mathrm{bCNOT}}\rho_{\mathrm{init}}\mathrm{U}^{\dagger}_{\mathrm{bCNOT}}\,, \tag{5.11}$$

after the bCNOT but before the post-selection.

Finally, the fidelity with respect to the ϕ^+ state in the polarisation DOF can be computed as

$$F_{\mathrm{pol,out}} = {}_{\mathrm{pol}}\langle\phi^+|\mathrm{tr}_{\mathrm{e-t}}\left\{\rho_{\mathrm{post}}\right\}|\phi^+\rangle_{\mathrm{pol}}\,, \tag{5.12}$$

where $\mathrm{tr}_{\mathrm{e-t}}$ is the partial trace over the e-t DOF.

5.3.2 Examples

As discussed in the previous section, it is in principle possible to produce noise independently in the two DOF. The noise can be produced about distinct axes and various combinations thereof. It would be desirable to test the ability of the setup to distil starting from a Werner like state in both DOF as this is the basis for the recurrence scheme proposed by BBPSSW [8]. But this is, if possible at all with this setup, experimentally challenging as the required configuration of the setup is not trivial. In addition, both, the distillation basin as well as the predicted maximal gain is small as shown in Figure 4.2. Not only is the controlled generation of Werner states challenging, but also the theoretical discussion is lengthy due to the large number of terms. Instead, the mathematical description will be illustrated using simpler examples.

One of the simplest, but still comprehensive, examples is the case of a bit flip in both DOF (BB), this is a mixture of ϕ^+ and ψ^+ states. The state incident on the PBS is then described by a product state of the two independent DOF as in equation (5.8)

$$\begin{aligned}\rho^{\mathrm{BB}}_{\mathrm{init}} &= \left[F_{\mathrm{pol}}|\phi^+\rangle_{\mathrm{pol}}\langle\phi^+| + (1-F_{\mathrm{pol}})\,|\psi^+\rangle_{\mathrm{pol}}\langle\psi^+|\right] \\ &\otimes \left[F_{\mathrm{e-t}}|\phi^+\rangle_{\mathrm{e-t}}\langle\phi^+| + (1-F_{\mathrm{e-t}})\,|\psi^+\rangle_{\mathrm{e-t}}\langle\psi^+|\right]\,.\end{aligned} \tag{5.13}$$

The four non-zero entries of this density matrix are on the diagonal. These entries can be found again in Table 5.3, which is an excerpt with the relevant rows from Table A.1. Additionally, the values of the entries are given in the column *fidelity*. While the first two rows remain unchanged, the permutation action of the bCNOT becomes apparent in the two bottom rows. The colour indicates both, the post-selection on the $\phi^\pm$ states and the quality of their contribution after the distillation process. Grey coloured rows indicate that the contributions

Table 5.3: *Action of bCNOT and post-selection in the case of a bit flip error in both DOF. Each row corresponds to an entry of the density matrix. While the values in the first column remain unchanged by the action of the bCNOT, the corresponding some positions in the density matrix are permuted. The entries before the bCNOT are given in the second and the third column, the entries after the bCNOT are given in the fourth and the fifth column. While the entries described by the first two rows remain unchanged by the action of the bCNOT, the entries described by the two bottom lines are swapped by the bCNOT. The grey coloured lines are discarded by postselection on the* $\phi^{\pm}$ *states in the energy-time DOF. The remaining contributions from the red and the green rows form the distilled ensemble.*

	before ($\rho^{\mathrm{BB}}_{\mathrm{init}}$)		after ($\rho^{\mathrm{BB}}_{\mathrm{bCNOT}}$)	
fidelity	control (pol)	target (e-t)	control (pol)	target (e-t)
$F_{\mathrm{pol}} F_{\mathrm{e-t}}$	ϕ^+	ϕ^+	ϕ^+	ϕ^+
$F_{\mathrm{pol}} \left(1 - F_{\mathrm{e-t}}\right)$	ϕ^+	ψ^+	ϕ^+	ψ^+
$\left(1 - F_{\mathrm{pol}}\right) F_{\mathrm{e-t}}$	ψ^+	ϕ^+	ψ^+	ψ^+
$\left(1 - F_{\mathrm{pol}}\right) \left(1 - F_{\mathrm{e-t}}\right)$	ψ^+	ψ^+	ψ^+	ϕ^+

are discarded because the e-t DOF is in a $\psi^{\pm}$ state after the bCNOT. Contributions in green and red coloured rows are kept, but only the contributions in the green row are beneficial for the distillation result as it contains a ϕ^+ state in the polarisation DOF. The state after post-selection is computed following equation (5.10). The resulting, normalised state is then

$$\rho^{\mathrm{BB}}_{\mathrm{post}} = \frac{F_{\mathrm{pol}} F_{\mathrm{e-t}} |\phi^+\rangle_{\mathrm{pol}}\langle\phi^+| + \left(1 - F_{\mathrm{pol}}\right)\left(1 - F_{\mathrm{e-t}}\right) |\psi^+\rangle_{\mathrm{pol}}\langle\psi^+|}{1 - F_{\mathrm{pol}} - F_{\mathrm{e-t}} + 2F_{\mathrm{pol}} F_{\mathrm{e-t}}} \,. \tag{5.14}$$

Due to the contributions from the red row, there is still a bit flip error present in the state after the post-selection $\rho^{\mathrm{BB}}_{\mathrm{post}}$. The output fidelity with respect to the ϕ^+ state in the polarisation DOF is then, following eq. (5.12),

$$F^{\mathrm{BB}}_{\mathrm{pol,out}} = \frac{F_{\mathrm{pol}} F_{\mathrm{e-t}}}{1 - F_{\mathrm{pol}} + F_{\mathrm{e-t}} \left(2F_{\mathrm{pol}} - 1\right)} \,, \tag{5.15}$$

where the nominator equals the yield.

The performance in case of the bit flip error in both DOF (BB) is illustrated in Figure 5.7. For the case of equal input fidelities in both DOF, the model for the Werner state in both DOF (WW) from Figure 4.2 is included for comparison. While the gain for BB is negative for all input fidelities below one half, it exceeds the gain for WW in the interesting region of input fidelities larger than one half. The maximal gain for BB is more than three times higher than for WW. Additionally, the distillation basin is much larger for BB than for WW and includes all possible combinations of input fidelities as long as they are both larger than one half.

A second example will be discussed in less detail. Getting closer to both a realistic scenario and the BBPSSW case, the performance for the case of a Werner state in polarisation and a

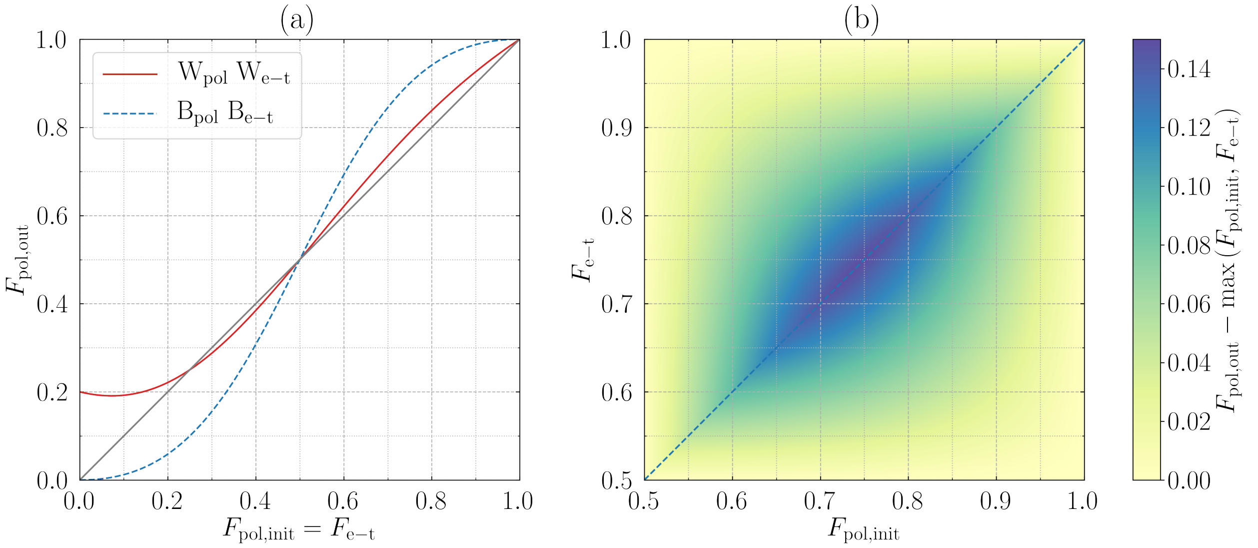

Figure 5.7: *Theoretical gain with respect to the maximal input fidelity for the case of a bit flip in both DOF. On the left (a) the case for equal input fidelities is shown. The previously discussed case of a Werner state in both DOF is included for comparison. The case for different input fidelities, shown on the right (b), is restricted to the region between* 0.5 *and* 1.

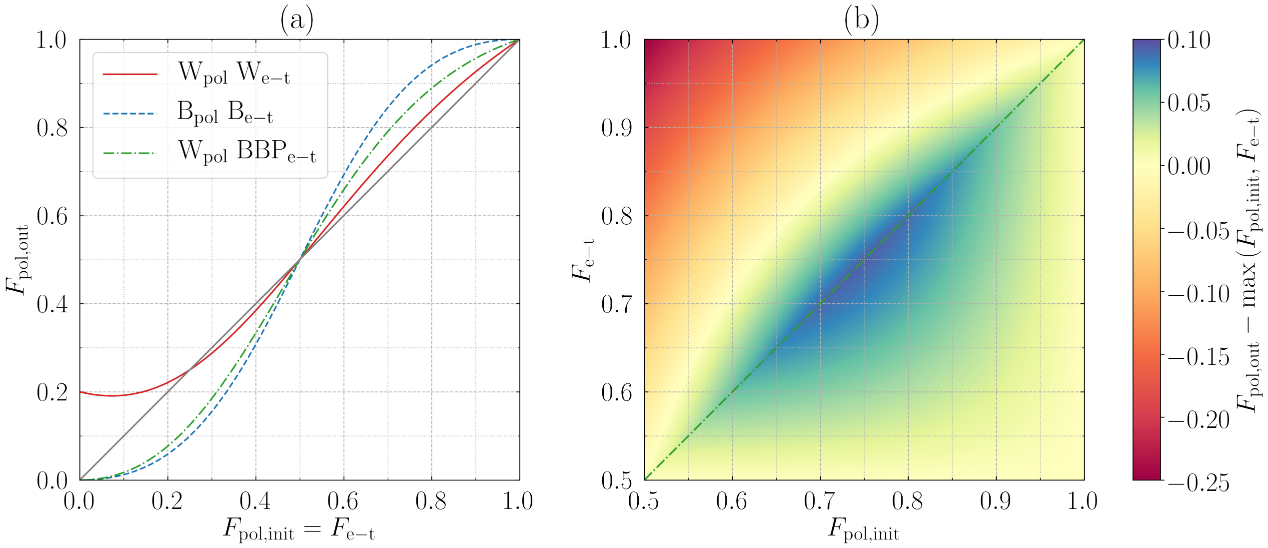

Figure 5.8: *Theoretical gain with respect to the maximal input fidelity for the case of a Werner state in polarisation and a bit flip and bit-phase flip error the e-t DOF. On the left (a) the case for equal input fidelities is shown. The previously discussed cases of a Werner state in both DOF and a bit flip error in both DOF is included for comparison. The case for different input fidelities, shown on the right (b), is restricted to the region between* 0.5 *and* 1.

bit flip as well as a bit-phase flip error in the e-t DOF (WBBP) is computed similarly to the previous example. The results of this simulation are shown in Figure 5.8 in the same manner as the previous simulations for WW and BB. The three different error models are compared for the case of equal input fidelities in both DOF. The overall behaviour of WBBP is similar to BB but the maximal gain is lower. Nevertheless, it is still more than twice the maximal gain of WW. For different input fidelities, different observations can be made for the region above and below the diagonal. Above the diagonal, a region of negative gain exist, that reach as far down as for WW. Below the diagonal, the gain is non-negative for all combinations of input fidelities above one half as it is for BB. Apparently, the gain in the region above the diagonal is governed by the state in the e-t DOF, while the gain in the region below is governed by the state in the polarisation DOF. In theory, the protocol does not make a difference between bit flip errors and bit-phase flip errors, so also the combination of both gives the same results. The poorer performance for WW compared to the other two scenarios is due to the phase flip contributions contained in white noise. A phase flip cannot be distilled directly with this protocol which manifests in a negative gain for all input fidelities above one half.

5.3.3 Experimental imperfections

So far, in the model everything has been assumed to be ideal and imperfections of components or alignment have not been taken into account. In the experiment, however, neither the state prepared by the source, nor the noise generation or the components and the alignment of the distillation setup are ideal. The reflection and transmission coefficients of the BS were measured, included in the model and the effect on the predicted gain was found to be in the sub per mill range. Of a similar magnitude is the influence of the PBS and their real performance acting as bCNOT at the heart of the protocol.

The input state, in contrast, does have a significant influence on the performance. Misalignment is the major issue for the initial polarisation state and introduces mainly bit flip and bit-phase flip contributions. Three delicate points are the power splitting ratio and the phase at the source, introduced in section 3.1, as well as the channel alignment with the polarisation controller pedals. The initial state in e-t is affected by the alignment of the Franson interferometer on the one hand. Both, non ideal path length differences as well as non perfect overlap of the spatial modes reduce the fidelity. On the other hand, the electronics of the stabilisation seems to introduce noise as slightly higher visibilities were observed with the interferometer free drifting. Nevertheless, the stabilisation is required for long term stability during the measurement.

In the adapted model the input state is assumed to be a Bell diagonal mixed state in each DOF. The fidelities are computed from the visibilities with the noisy channel set to neutral and the coincidence window restricted to the central peak. Because the misalignment, and so the visibilities of the input state vary between the measurement days, the input state has to be readjusted for each measurement run.

Not yet included in the model is the real performance of the noisy channel as well as the role of phase compensation after the PBS. The noise generation is assumed as perfect rotations about the axes. While it would be manageable to do the computations for the examples presented in the previous section by hand, the model including at least some experimental imperfections is too complex to be computed manually. Analytic results were computed with Wolfram Mathematica. These results were used to generate plots with Python shown and discussed in comparison with the experimental data in section 6.

5.4 Experimental setup

An overview over the full experimental setup is given in Figure 5.9. Actually, the setup is never used in the shown configuration, but some of the removable components are always taken out depending on the fidelity that is to be measured. A more detailed discussion on the three configurations follows in section 5.5.

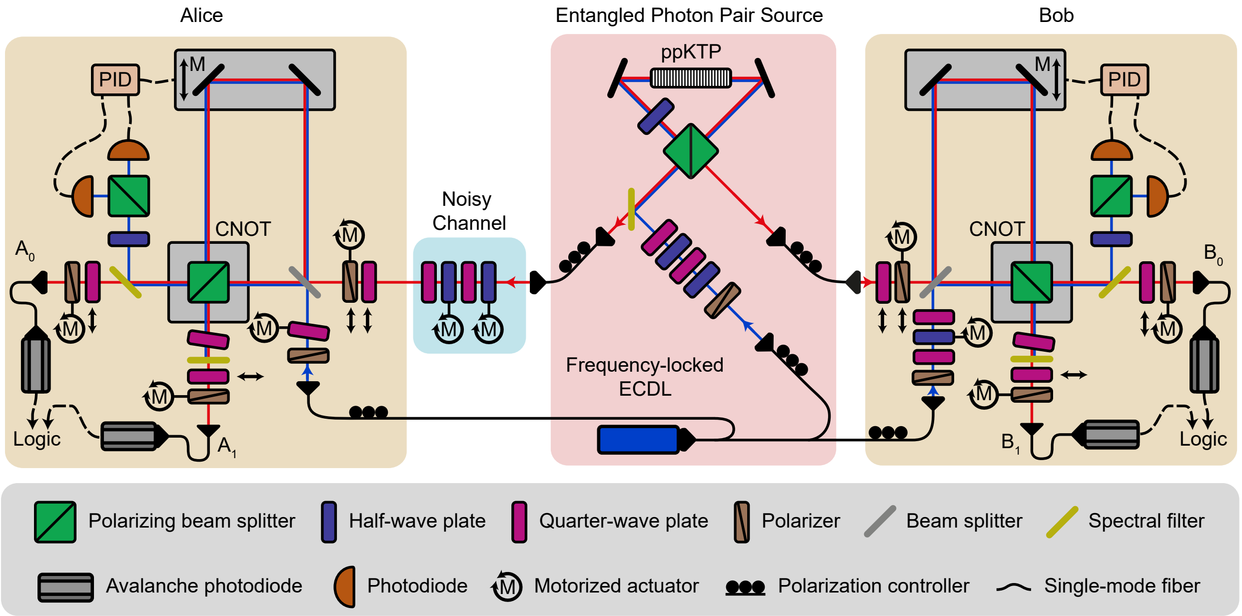

Figure 5.9: *Schematic of the full experimental setup for single-copy entanglement distillation. The building blocks are the entangled photon pair source, the noisy channel and the two arms of the Franson type interferometer. Additionally, the active stabilisation with the pump laser, the polarisation controllers for channel alignment as well as polarisers and wave plates for various measurements discussed in the text are included in this figure. The components next to two-sided arrows are removable.*

The basic structure is the same modified Franson interferometer as shown in the simplified version of the setup in Figure 5.2.

In addition to the passive stabilisation by a cardboard box covering the optical table with the Franson-type interferometer, also an active stabilisation is required for the long term stability throughout a measurement. For this purpose, the same frequency-locked external grating diode laser (ECDL) that is employed as pump laser for the source is used. It enters each unbalanced Mach-Zehnder interferometer on the remaining input port of the BS, propagates along the same paths as the single photons and is filtered out by spectral filters after the PBS. One of these spectral filters is a dichroic mirror that redirects the stabilisation laser to a HWP set at $\pi/8$ followed by a PBS. This combination erases the which-path information and so allows the photodiodes to detect an interference signal. The signal of the two photodiodes is subtracted and then processed by a proportional-integral-derivative controller (PID) which returns a feedback signal to the piezoelectric actuator moving the translation stage.

For the detection of the single photons, Excillitas avalanche photodiodes[1] are used. The signals from the detectors are recorded with the time tagging module Swabian instruments Time Tagger Ultra and saved as raw data. At a later time, with the relative delays between the channels set, this raw data is analysed by a coincidence logic. The software for handling the output of the time tagging module was kindly provided and adapted to the needs of the experiment by Lukas Bulla and Jan Lang. This includes both, the software for the live view during the experiment and the coincidence logic employing the so called ladder algorithm. Further post-processing is done with Python.

In the following, the setup and central alignment steps of both source and Franson type interferometer will be explained in more detail.

5.4.1 Entangled photon pair source

The source has already been used in this configuration for other experiments. So, coarse realignment was only necessary after cleaning and replacement of single components. For this, the active support of Jan Lang and Lukas Bulla was very helpful. Otherwise, only fine tuning was necessary before each distillation measurement day to ensure a high fidelity input state.

The SPDC source is set up in Sagnac configuration, introduced in section 3.2, with a type-II phase-matched ppKTP crystal with collinear emission. Here the setup of the source is described starting from the pump laser. The pump laser is the same ECDL at 405 nm as used for the stabilisation coupled to a single-mode fibre to clean the spatial mode. With the polarisation controller pedals followed by a polariser set at H the pump laser power can be controlled without affecting the frequency of the laser. The HQHQ channel gives full control over the polarisation state of the pump laser. With the first HWP the state is rotated in the linear basis and so the power splitting ratio at the PBS in the Sagnac loop can be controlled. The QWP are set at $\pi/4$ such that the phase of the pump state and so the phase of the resulting single photon state can be controlled with the second HWP as discussed in section 3.2. By coupling the single photons to single-mode fibres, indistinguishability in spatial modes is ensured.

---

[1] To be more precise, type SPCM-800-11-FC with serial number 29865 (A0) and 29863 (A1) and type SPCM-AQRH-14-FC with serial numbers 26740 (B0) and 26739 (B1) are used.

Before the crystal is inserted into the loop, the loop is aligned such that it mimics a retro-reflecting mirror for both propagation directions of the blue pump laser. For easier alignment of the loop a Faraday rotator and a PBS are added right in front of the laser. This modification allows to maximise the back-coupling to the single-mode fibre at the same time as the 0th order interference on a screen is minimised. At this point, the first HWP determining the power splitting is set. A good value for the back-coupling is found to be a quarter of the input pump power. When the loop is set and the crystal is inserted into the loop the translation DOF and the rotational DOF of the crystal are roughly aligned. The translation DOF are aligned with respect to the back-coupling, while the rotation DOF are aligned with respect to the interference on the screen. By manipulating all DOF of the collimators, that couple the single photons to the single-mode fibre, iteratively, first the local counts, then the coincidence counts and the heralding are maximised. Fine tuning is then done by minimal changes of the crystal position.

Locally the desired state is set only with the HQHQ channel iteratively rotating the two HWP. The visibilities in the linear bases are measured with polarisers inserted right in front of the single photon collimators. To obtain the desired input state at the distillation setup, the channels from the source to the Franson type interferometer have to be aligned. First, a bit flip is introduced in one of the channels in order to transform ψ states generated by the type-II source to ϕ states received at the Franson type interferometer. At the source, the polarisers are set arbitrarily in the H/V basis. In one arm, the input polariser at the distillation setup is adjusted orthogonally with respect to the polariser in the same arm at the source. In the other arm, the input polariser is set parallel to the corresponding polariser at the source. The long arms are blocked and the polarisers after PBS are set to H in the A0 and B0 ports and to V in the A1 and B1 ports. With the polarisation controller pedals the local counts at A and B are minimised. In a second step, the phase and the balance are adjusted with the HQHQ channel at the source. For this the polarisers at the source are removed and the input polarisers at the distillation setup are set to D and A respectively. By minimising the coincidence counts again, the target state ϕ^+ is set, which is required for the distillation process and exhibits correlations in both linear bases.

5.4.2 Distillation setup

The final distillation setup is shown in Figure 5.10. Unlike the schematic setup in Figure 5.9 might suggest, the complete Franson type interferometer is fit on one optical table.

In contrast to the source, the Franson type interferometer used for distillation was built from scratch. The alignment of the setup pursues two principal objectives. Firstly, a good spatial mode overlap has to be ensured in each Mach-Zehnder interferometer even when the translation stage is moved or polarisers or wave plates are rotated. This includes that the single-mode coupling after the interferometer should not be affected by different measurement

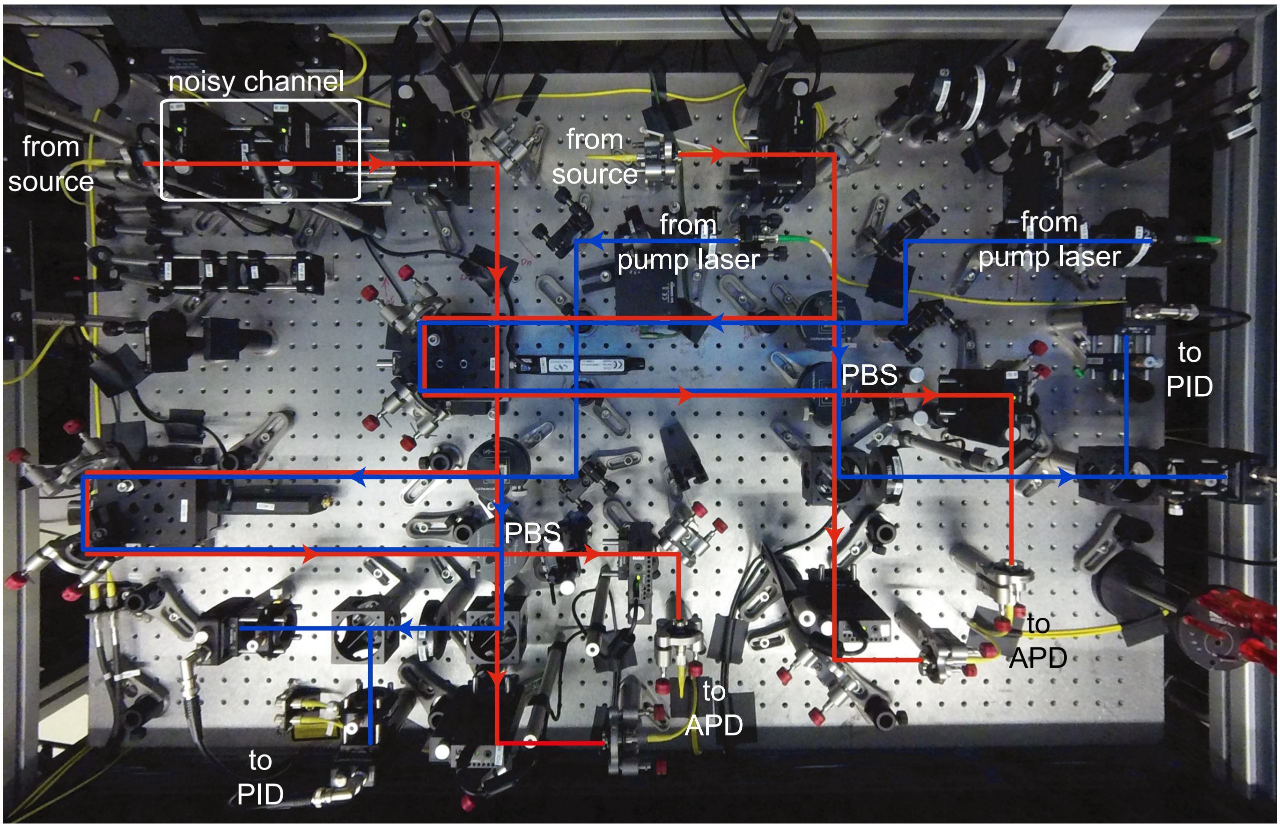

Figure 5.10: *Photography of the modified Franson interferometer in the lab. The blue and red lines illustrate the propagation paths of the pump laser and the single photons respectively. The imbalance of the Mach-Zehnder interferometers causes a temporal delay of approximately* 2.6 ns.

settings. Secondly, the polarisation has to be maintained until it is analysed and crosstalk between the DOF has to be prevented.

The unbalanced Mach-Zehnder (MZ) interferometers are aligned individually with an 810 nm alignment laser. In a first step, pinholes aligned to the height of the laser beam right after the collimator are used to align mirrors and BS such that the propagation paths strictly follow the hole grid of the optical table. This ensures reflections through an angle of 90° and is beneficial for both main objectives stated before. In connection with the use of silver coated mirrors, the polarisation is not disturbed in an uncontrolled fashion. Furthermore, moving the translation stages does neither affect the mode overlap nor the single-mode coupling. The spatial mode can also be affected by the rotation of wedged polarisers or wave plates, causing varying transversal walk-off. Because this can severely affect the coupling from free space to the single-mode fibre, the components with the least wedge are selected from the batch. With the polarisers before and after the MZ interferometer set to D interference is observed in both output ports. With the translation stage moving at the lowest possible motor speed and an Ophir Spiricon beam profiler in the one arm and a power meter in the other arm, the visibility of the free space interference is maximised. This is done by fine adjustment of the two mirrors in the long path. While the free-space visibility usually exceeds 97 %, the visibility after coupling to single-mode fibre reaches up to 99 %. The relative phase between H and V components is corrected with tilted QWP in the output ports A1 and B1 with respect to the output ports A0 and B0 to ensure that the interference fringes in the two ports are in phase.

When the alignment of the 810 nm modes is finished, the components for the stabilisation with the blue pump laser are aligned. The components of the interferometer are not touched again, but the interference visibility of the stabilisation laser is maximised with the two mirrors before the interferometer. The demands are not as high as for the single photons, because a visibility of 90 % is sufficient for the PID controllers to work properly and the photo diodes have a large detection area. The signal of the photo diodes is directed to both, an oscilloscope for screening during a measurement and an analogue subtractor including a low pass filter provided and installed by Lukas Bulla. The parameters of the PID are set following no certain procedure but such that the target position is reached in a reasonable time and the system is stable over hours. The setup is stable over days and only very little realignment of the mirrors in the long paths is required to prepare the interferometer for a measurement day.

5.5 Determine the fidelity

The fidelity cannot be measured directly, but is computed from visibilities in three different bases. These visibilities are in turn computed from coincidence counts with parallel and orthogonal analyser settings as discussed in section 2.3. Often, a lower bound for the fidelity $\left(|V_{\mathrm{xx}}| + |V_{\mathrm{zz}}|\right)/2 \leq F$ is computed with the visibilities in the linear bases. This turns out to be not sufficient for this experiment. As discussed before, each isolated noise model corresponds to a rotation about an axis. While the visibilities in bases that are in the plane of rotation are increased or reduced due to the rotation, the visibility in the basis along the rotation axis does not change. Therefore, the bound is exact for rotations about the x-axis and about the z-axis, but it is far off for rotations about the y-axis. A rotation about the y-axis results in a bit-phase error, so the visibilities depend on the fidelity like

$$\begin{aligned} & V_{kk}\left(F|\phi^{+}\rangle\langle\phi^{+}| + (1-F)\,|\psi^{-}\rangle\langle\psi^{-}|\right) \\ =& \mathrm{tr}\left\{(\sigma_k\otimes\sigma_k)\left((2F-1)\,\sigma_{\mathrm{x}}\otimes\sigma_{\mathrm{x}} - \sigma_{\mathrm{y}}\otimes\sigma_{\mathrm{y}} + (2F-1)\,\sigma_{\mathrm{z}}\otimes\sigma_{\mathrm{z}}\right)\right\} \end{aligned} \tag{5.16a}$$

$$= \begin{cases} 2F-1\,, & \text{for} \quad k=z \\ -1\,, & \text{for} \quad k=y \\ 2F-1\,, & \text{for} \quad k=z \end{cases} . \tag{5.16b}$$

With an underestimated fidelity it is not possible to properly asses the performance of the distillation process. As a consequence, the visibilities along all three axes have to be measured such that the fidelity can be computed exactly following equation (2.16). In Figure 5.11 both, the measured polarisation input visibilities used to compute the fidelity and the corresponding theoretical prediction are plotted for the example of a bit flip error, i.e. a rotation about the x-axis. The overall agreement is good. The visibility in D/A is slightly below unity, and the H/V visibility is always above the predicted value. While the non-perfect input state is considered as a parameter in the model, the noisy channel is not. Minor misalignment of the four wave plates accumulates to the deviation from the model in Figure 5.11.

For a full measurement, each data point is composed of three fidelitites. Firstly, this is the initial polarisation fidelity $F_{\mathrm{pol,init}}$. It in includes both, the intentional reduction of the fidelity by the noisy channel, and the reduction due to a non-ideal input state as well as misalignment of the noisy channel. Secondly, this is the other fidelity of the input state, the energy-time fidelity $F_{\mathrm{e-t,init}}$. Even though this fidelity should not change for different settings of the noisy channel, it is measured for each setting. Thirdly, this is the polarisation fidelity of the output state after the distillation step $F_{\mathrm{pol,out}}$. Set in relation to the input fidelities, the output fidelity allows to evaluate the performance of the setup. For the different measurements the configuration of the setup is varied slightly.

5.5.1 Fidelity in Polarisation

For the measurements concerning the input polarisation, the motorised polarisers after the noisy channel, but before the interferometers are inserted as shown in Figure 5.12. The QWP are inserted as well for measurements in the circular basis and they are removed for measurements in the linear bases. Since the projection on a certain polarisation state takes place at the polarisers, the rest of the interferometer works as a bucket detector and should collect all

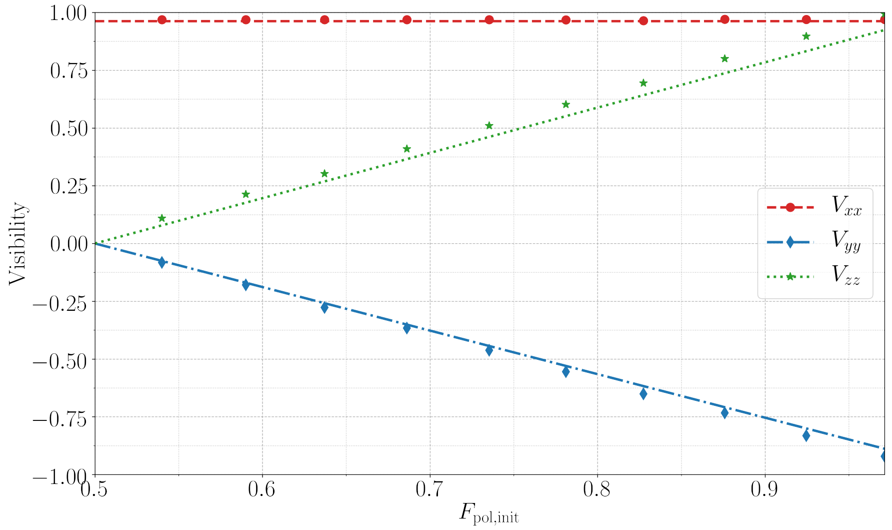

Figure 5.11: *Visibility of the input polarisation state for a rotation about the* x*-axis plotted over the input polarisation fidelity* $F_{\text{pol,init}}$*. The theoretical lines are plotted in a colour matching the markers that indicate measured values. The experimental data is accidental count corrected and the error bars originating from the counting statistics are too small to be displayed. The subscripts in the legend refer to the axes of the Bloch sphere, e.g.* V_{xx} *is the visibility for* A *and* B *measuring in the* D/A *basis.*

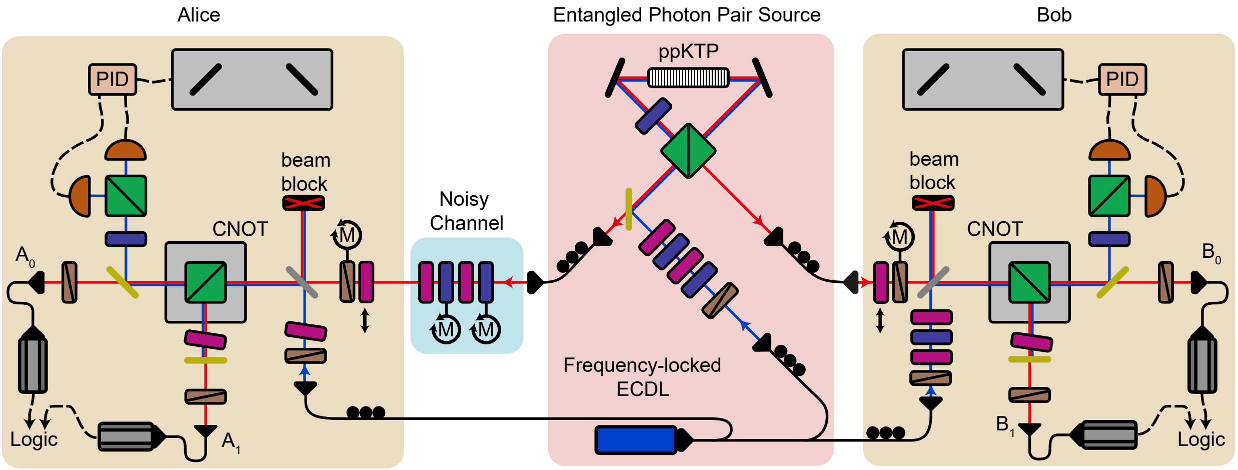

Figure 5.12: *Setup configuration for measurement of input polarisation fidelity. The polarisation analysers are set directly after the channels and the interferometer is reduced to two bucket detectors. An active stabilisation is not required. This a reduced version of the full setup shown in Figure 5.9, so the same legend applies and it is not shown here again.*

transmitted photons. While there is no polarisation entanglement after the polarisers, energy time entanglement is still present and would lead to interference effects if not one of the paths were blocked. The long path is blocked, as the losses are smaller in the short path. With only the short paths working, there are no interferometers to stabilise, so the active stabilisation can be switched off. Since the polarisers after the PBS cannot be removed, they are set to H and V in the transmitted paths ($\mathrm{S}'_\mathrm{A}/\mathrm{S}'_\mathrm{B}$) and the reflected paths ($\mathrm{L}'_\mathrm{A}/\mathrm{L}'_\mathrm{A}$) respectively. The coincidence counts for the four channel combinations are processed and added thereafter. Per initial polarisation fidelity, measurements are required at 24 different settings, each with an integration time of 10 s.

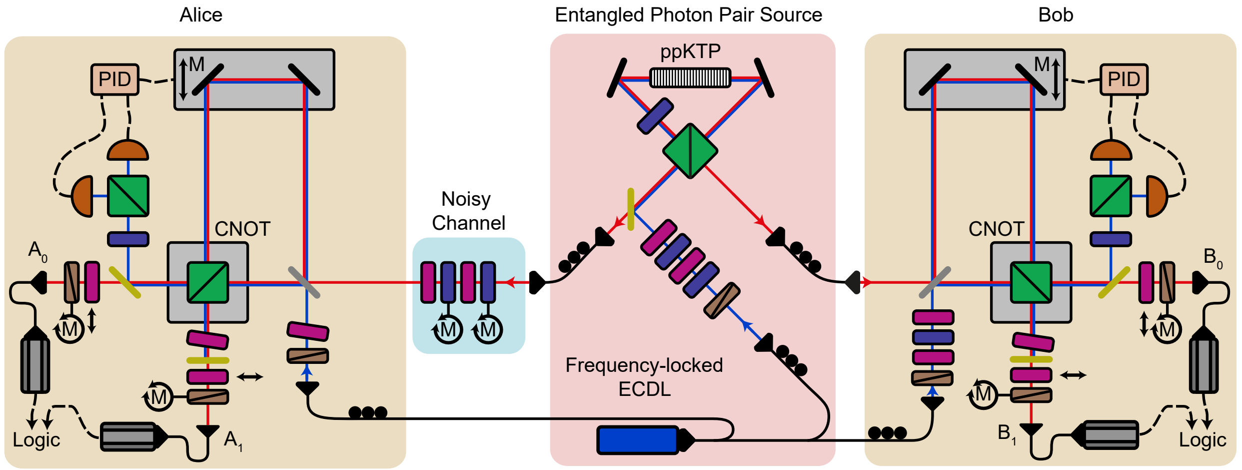

Figure 5.13: *Setup configuration for measurement of output polarisation fidelity. All components are needed but the polarisers and QWP before the interferometer. This a reduced version of the full setup shown in Figure 5.9, so the same legend applies and it is not shown here again.*

The measurements for the output polarisation fidelity are more demanding than the measurements for the input polarisation fidelity. The long paths are unblocked and the active stabilisation is employed, because phase stability is required. The polarisers and the QWP before the interferometer are removed such that the noisy polarisation state is forwarded to the distillation interferometer. While going through all the polariser combinations in the bases, the polarisers on one side are always in the same setting, as only coincidences between Alice and Bob are of interest. By considering only coincidences between S'_A and S'_B as well as L'_A and L'_A, the post-selection on $\phi^\pm$ states in the e-t DOF is realised. Similarly to the input polarisation fidelity, 24 different settings are required per data point.

5.5.2 Fidelity in energy-time

In contrast to the four required configurations per basis for polarisation measurements, only one configuration per basis is required for energy-time measurements. This sums up to six settings per initial polarisation fidelity. To compute the visibility, the coincidence counts

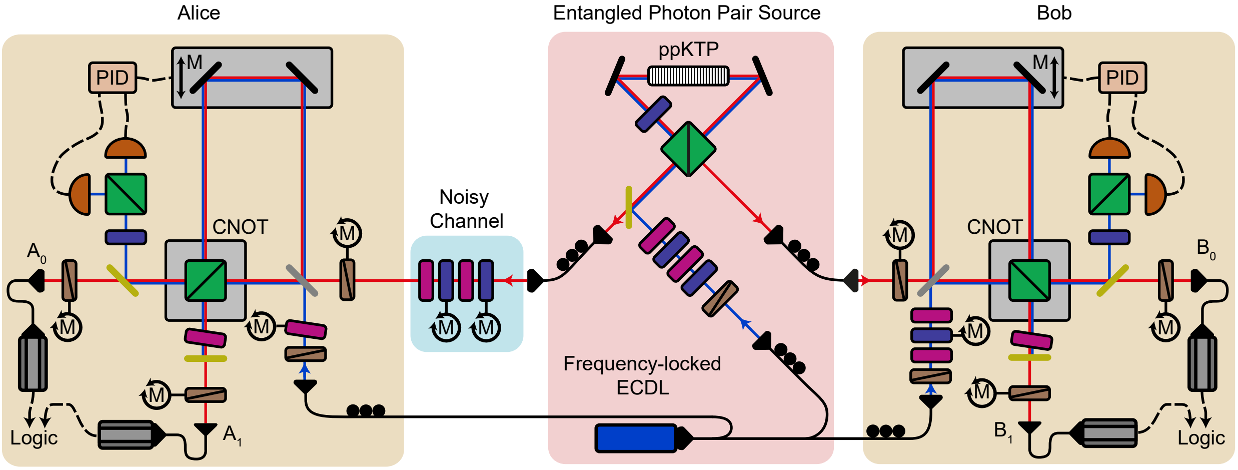

Figure 5.14: *Setup configuration for measurement of energy-time fidelity. All polarisers are inserted and all QWP are removed. The polarisers and the phase control of the stabilisation laser are used to set the basis. This a reduced version of the full setup shown in Figure 5.9, so the same legend applies and it is not shown here again.*

between the same PBS output modes, that is S'_A and S'_B as well as S'_A and L'_A are subtracted from those between opposite output modes. All polarisers are inserted, so the states entering the interferometer are not entangled in polarisation anymore. For the first basis, the so called time of arrival basis, all polarisers are set to H, so there should be only transmission at the PBS and the signals at the detectors can be associated with the paths taken by the photons. Photons reflected by the BS take the long path and are detected in the one output ($\mathrm{L}'_\mathrm{A}/\mathrm{L}'_\mathrm{A}$), while photons transmitted by the BS are detected in the other output ($\mathrm{S}'_\mathrm{A}/\mathrm{S}'_\mathrm{B}$). There are no interference effects, so active stabilisation is not required. By setting all polarisers on D, a superposition basis can be measured. The polarisers after the PBS delete the path information such that interference can be observed in the e-t DOF. The configuration for the second superposition basis is realised by introducing a phase shift in the long paths. This phase shift is controlled by manipulating the polarisation state of the stabilisation laser. Because the same laser is used for pumping the SPDC source and the stabilisation, it is of exactly half the wavelength of the single photons. By tilting a QWP at Alice's side and rotating the HWP of the QHQ channel at Bob's side, a phase shift of π is introduced for the laser in the imbalanced Mach-Zehnder interferometer. This introduces a phase shift of $\pi/2$ for the single photons in the long paths.

6 Results and discussion

The distillation basin for a bit flip error in polarisation and a bit flip and bit-phase flip error in the e-t DOF reaches at least from a fidelity $F_{\mathrm{e-t}} = 0.5135(12)$ to a fidelity $F_{\mathrm{e-t}} = 0.9352(7)$ in the energy-time DOF. This is a lower bound for the region of positive gain as no measurement data exists at the extremal points of the basin. The maximally measured total gain in fidelity is

$$\left(F_{\mathrm{pol,out}} - \max\left(F_{\mathrm{pol,init}}, F_{\mathrm{e-t}}\right)\right)_{\max} = 0.1031(9)\,, \tag{6.1}$$

at $F_{\mathrm{pol,init}} = 0.7344(8)$, $F_{\mathrm{e-t}} = 0.7344(11)$ and a yield of $Y = 0.6317(6)$. The error is computed by Gaussian error propagation of the standard deviation of the Poissonian counting statistics.

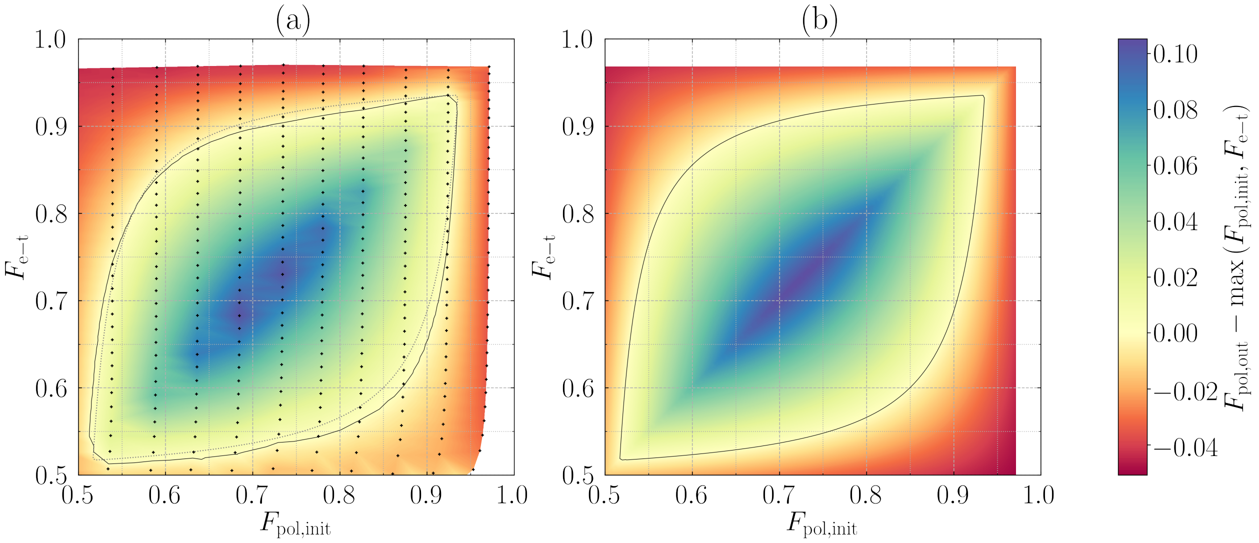

Figure 6.1: *Heatmaps of the gain in polarisation fidelity with respect to the maximal input fidelity in experiment (a) and theory (b). Accidental corrected measured data points are indicated by markers. In total the data points are the result of 594 single measurement settings. The lines are drawn at zero gain. The dotted line in the experimental plot is the theoretical zero line for comparison. The same normalisation and the same colour map applies to both frames.*

The heatmaps in Figure 6.1 give an impression of the performance of the setup for a bit flip error in polarisation and a bit and bit-phase flip error in the e-t DOF. On the axes, the input fidelity in polarisation and energy-time are depicted. The markers in the left plot indicate measured data points and the colour represents the gain in polarisation fidelity with respect to the maximal input fidelity for each point. The spacing of the grid of data points is determined vertically by the coincidence windows chosen in post-processing. The horizontal spacing is determined by the noisy channel settings during the experiment. In total, 594 single measurements, each with 10 s integration time, were conducted to obtain the data presented in Figure 6.1. Between the measurement points the gain is interpolated using triangulation and linear interpolation. The distillation basin is limited by the line of zero gain, which is indicated by a solid line in each plot. In the plot of the experimental data, the theoretical zero gain line is included as a dashed line for comparison. Close to unit input fidelities, there is a white region that could not be reached with the input states.

The model takes the imperfect input state into account, and so predicts the overall behaviour much better than the ideal model discussed in section 5.3.2. The information about the input state is gained from the data point with neutral HQHQ setting and narrow coincidence window. This is the point with the largest fidelity in both DOF. In the plots this corresponds to the top most right point. In contrast to the ideal case, regions of negative gain are predicted even for input fidelities larger than one half and the distillation basin is not symmetric about the diagonal.

The points for a fixed coincidence window fluctuate around a horizontal line for different noisy channel settings. This may be caused by a variation of the single-mode coupling efficiency with the position of the wave plates in the noisy channel due to wedging. A different behaviour can be observed for fixed noisy channel settings and various coincidence windows. In principle it would be expected to find the markers on a straight vertical line. This is not the case. The polarisation input fidelity decreases with the e-t input fidelity and so with an increasing coincidence window. Most severely, this can be observed for high polarisation input fidelities as they are most fragile. This indicates a crosstalk between the polarisation DOF and the energy-time DOF, such that the two DOF cannot be manipulated completely independently. A possible cause of this crosstalk was observed at the source. Due to reflections within the source, side peaks with correlations opposite to the correlation dominating the central peak of coincidence counts are observed. When the coincidence window is widened, not only the side peaks of the Franson-type interferometer are included, but also the side peaks originating from the source. The sudden increase of the deviation from the vertical line for low e-t input fidelities can be explained by the fact that the side peaks caused by reflections in the source are slightly further away from the central peak than the side peaks of the Franson interferometer. More details on the source side peaks can be found in appendix A.5. The bit flip and bit-phase flip errors introduced by the crosstalk, however, do not explain the gain reached in the experiment in the region of small e-t and large polarisation input fidelities, which is larger than predicted by the model.

While the overall shape of the distillation basins agree, the theoretical basin exceeds the experimental basin for high e-t fidelities and it is smaller than the experimental basin for e-t fidelities below 0.8.

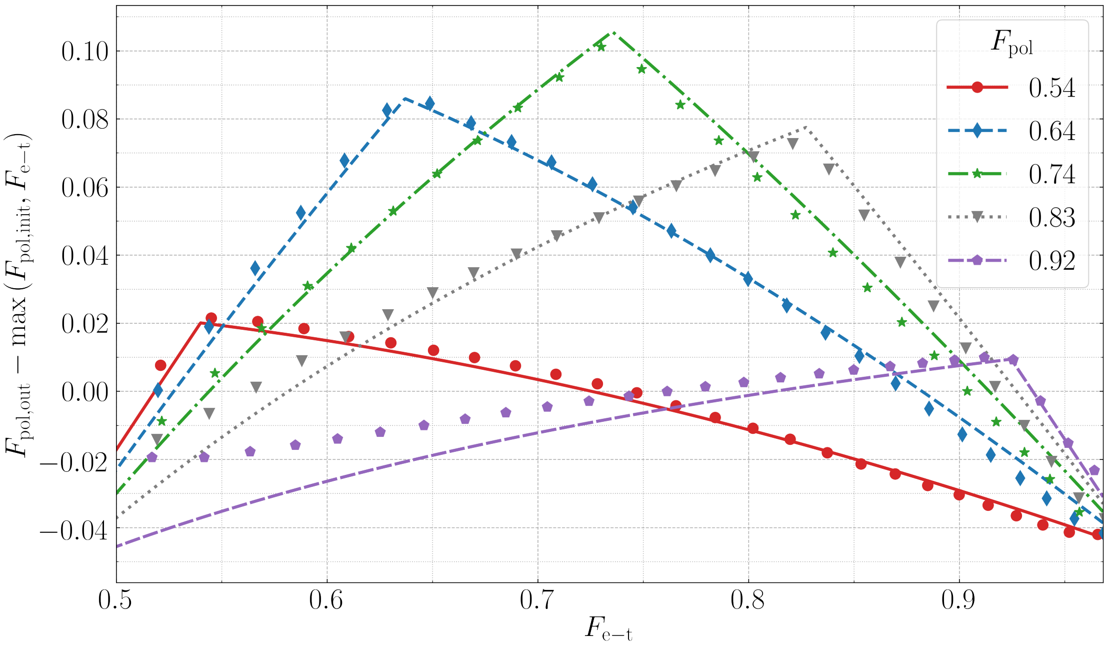

Figure 6.2: *Gain plotted for various constant input polarisation fidelities. For each cut the lines and markers of the same colour represent theoretical and experimental data respectively. The plot should be treated with care as the experimental and the theoretical cuts do not agree exactly.*

The heatmaps in Figure 6.1 do not allow for a direct comparison of experimental data and theoretical model as they are side by side. A direct comparison is not that easy, because the model takes the imperfect input state into account but considers the noise generation in both DOF as ideal. As a result cuts through the heatmaps for fixed input fidelities are easy in the model, which is not the case in the experiment, as discussed in the previous paragraph. Therefore cuts through the heatmaps for constant input fidelities should be treated carefully. The experimental and the theoretical cuts for a constant input polarisation fidelity shown in Figure 6.2 overlap only at the maximal energy-time fidelity and diverge towards lower e-t fidelity. Not only the region of positive gain is shown, but the ordinate reaches to negative gain. Both, for an e-t fidelity close to 0.5 and close to 1 the gain is negative regardless of the polarisation fidelity. The weakness of the model becomes most apparent again for small e-t fidelities and large pol fidelities.

The cuts for the extremal e-t fidelities in Figure 6.3 are below zero gain for all polarisation fidelities, since the distillation basin is not cut. Otherwise, similar observations as for the cuts for constant polarisation fidelities can be made.

By employing the energy-time DOF, the yield in the polarisation DOF is boosted and reaches up to 1. In Figure 6.4 the experimentally achieved yield as well as the theoretically predicted

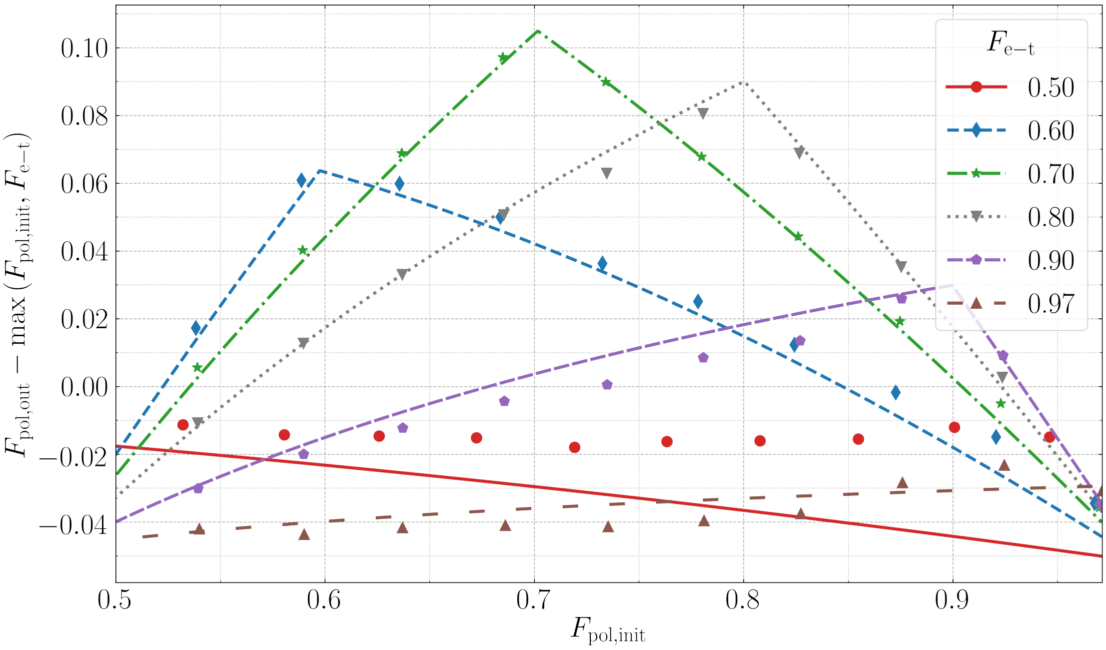

Figure 6.3: *Gain plotted for various constant input energy-time fidelities. For each cut the lines and markers of the same colour represent theoretical and experimental data respectively. The plot should be treated with care as the experimental and the theoretical cuts do not agree exactly.*

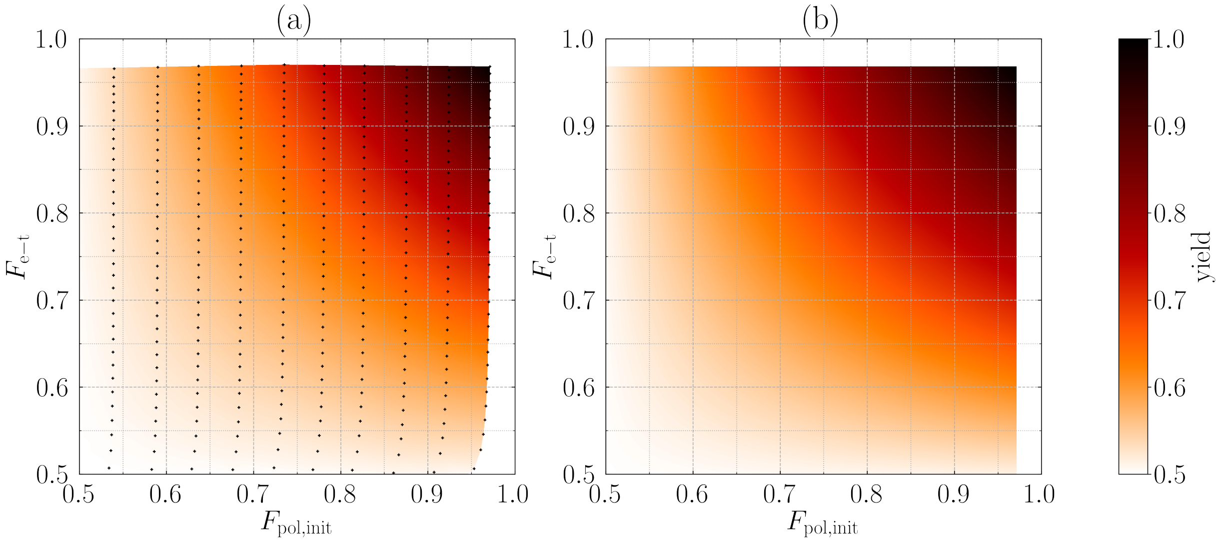

Figure 6.4: *Yield in the polarisation DOF plotted from experimental data (a) and from the theoretical model (b). The markers in (a) indicate measured data points. The colour indicates the obtained yield, this is the number of output states divided by the number of input states in polarisation. Between the data points triangulation and linear interpolation is used.*

yield is shown. It is maximal for high input fidelities in both DOF and decreases to 0.5 with the input fidelities.

7 Conclusions and outlook

In this proof of principle experiment of entanglement distillation using passive linear optics and photons hyperentangled in the polarisation and the energy time DOF a gain that is positive by up to 114 standard deviations has been obtained.

It has been demonstrated, that distinct errors can be introduced and controlled by a comb of wave plates in the polarisation DOF and by including the non-interfering background in the energy-time DOF. In both DOF the visibility has been measured in three mutually unbiased bases in order to determine the Bell state fidelity exactly. The demand of phase stability on the order of the wavelength of the two unbalanced Mach-Zehnder interferometers has been met such that high energy-time fidelities could be measured and successful distillation could be performed. A maximal total gain of more than 10 % for a bit flip error in the polarisation DOF and a bit and bitphase flip error in energy-time DOF has been reached. The overall behaviour of the experimental results can be described by a model that takes the experimental input state into account. Cross talk between the DOF and the phase compensation are not yet considered in the model. Including this as well might improve the model further.

Based on this experiment, further experiments can be performed. Some require no or little modifications of the setup, others require more effort. As the setup is at the moment, various error models can be tested. Aside from a bit flip error the noisy channel can also produce phase flip and bit-phase flip errors. While a phase flip error alone is not too interesting as only negative gain is predicted and a bit-phase flip error is expected to give the same results as the bit flip error described in this work, they can all be combined resulting in a Werner state in polarisation. Other ways to produce a Werner state in polarisation may include heating and mechanically twisting the fibres.

Full quantum state tomography would allow deeper insights in the performance of the setup and theoretical hypotheses could be tested. The purity could be computed and used as a verification that the input state actually is a mixed state. While the fidelity is a lower bound for entanglement, a real entanglement measure such as the concurrence could be computed. Additionally, it could be verified that the Schur product relates the density matrices of the input and the output states.

The proposed pumping scheme DEPP [66] can easily be implemented by inserting dual wavelength HWP in the long paths before the PBS. This way bit flip and phase flip errors can be treated in one step.

Considerable modifications of the setup are required to add more dimensions to the analysis of the energy-time DOF. For this, more possible paths of different length are required. In principle more DOF could be employed, such that more than one distillation step could be performed. Already with two steps also the phase flip error could be purified following the BBPSSW scheme. Prerequisite for the expansion to more DOF is the feasibility of the generation of hyperentanglement in those additional DOF and of an efficient implementation of the CNOT gate between the DOF.

Both the polarisation and the e-t DOF have been proven suitable for entanglement distribution under real conditions via free-space [52] as well as fibre [67, 68]. In the long term, it would be desirable to bring distillation protocols out of the lab and test them under field conditions.

While writing this thesis, the results of this experiment as well as a closely related experiment were published [69, 70].

Appendix

A.1 Fidelity and visibility

The visibility along an axis k with $k \in \{x, y, z\}$ of a two qubit state in Bloch representation computes as

$$V_{kk}\left(\rho^{(2)}_{Bloch}\right) = \mathrm{tr}\left\{\frac{1}{4}\left(\mathbb{1}_2 \otimes \mathbb{1}_2 + a_i\sigma_i \otimes \mathbb{1}_2 + b_i\mathbb{1}_2 \otimes \sigma_i + t_{ij}\sigma_i \otimes \sigma_j\right) \cdot \sigma_k \otimes \sigma_k\right\} \tag{A.1a}$$

$$\begin{aligned} &= \frac{1}{4}\left(\mathrm{tr}\left\{\left(\mathbb{1}_2 \otimes \mathbb{1}_2\right)\left(\sigma_k \otimes \sigma_k\right)\right\} + a_i\mathrm{tr}\left\{\left(\sigma_i \otimes \mathbb{1}_2\right)\left(\sigma_k \otimes \sigma_k\right)\right\}\right. \\ &\qquad \left. + b_i\mathrm{tr}\left\{\left(\mathbb{1}_2 \otimes \sigma_i\right)\left(\sigma_k \otimes \sigma_k\right)\right\} + t_{ij}\mathrm{tr}\left\{\left(\sigma_i \otimes \sigma_j\right)\left(\sigma_k \otimes \sigma_k\right)\right\}\right) , \end{aligned} \tag{A.1b}$$

with $(A \otimes B)(C \otimes D) = AC \otimes BD$ and $\mathrm{tr}\{A \otimes B\} = \mathrm{tr}\{A\}\,\mathrm{tr}\{B\}$,

$$\begin{aligned} &= \frac{1}{4}\Big(\mathrm{tr}\left\{\sigma_k\right\}^2 + a_i\mathrm{tr}\left\{\sigma_i\sigma_k\right\}\mathrm{tr}\left\{\sigma_k\right\} + b_i\mathrm{tr}\left\{\sigma_k\right\}\mathrm{tr}\left\{\sigma_i\sigma_k\right\} \\ &\qquad + t_{ij}\mathrm{tr}\left\{\sigma_i\sigma_k\right\}\mathrm{tr}\left\{\sigma_j\sigma_k\right\}\ \Big) , \end{aligned} \tag{A.1c}$$

with $\mathrm{tr}\{\sigma_i\} = 0$ and $\sigma_i\sigma_j = \delta_{ij}\mathbb{1}_2 + \mathrm{i}\sum_{k\in\{x,y,z\}} \epsilon_{ijk}\sigma_k$,

$$= \frac{1}{4}t_{ij}\delta_{ik}\delta_{jk}\mathrm{tr}\left\{\mathbb{1}_2\right\}^2 = \frac{1}{4}t_{kk}2^2 \tag{A.1d}$$

$$= t_{kk}\,. \tag{A.1e}$$

A.2 Bilateral CNOT

In the Bell basis $\{\phi^+, \psi^+, \phi^-, \psi^-\}$ the action of the bCNOT can be described by the 16×16 permutation matrix

$$\mathrm{U_{bCNOT}} = \mathbb{1}_2 \otimes \mathrm{diag}\left(\mathbb{1}_2, 0_2, \sigma_\mathrm{x}, 0_2\right) + \sigma_\mathrm{x} \otimes \mathrm{diag}\left(0_2, \mathbb{1}_2, 0_2, \sigma_\mathrm{x}\right) , \tag{A.2}$$

where $\mathbb{1}_2$ and 0_2 denote the 2D identity and the 2D zero matrix respectively. σ_x is the Pauli-x matrix. An overview of the action of the bCNOT can be found in Table A.1 . A CNOT gate followed by a measurement of the target qubit is a parity measurement. Similarly the bCNOT followed by a correlation measurement of the target state in the computational basis can be

Table A.1: *Action of the bilateral CNOT gate on Bell states with the polarisation DOF as source qubit and the spatio-temporal DOF as target qubit. The combinations in the left two columns are transformed to the combinations in the same row in the right two columns.*

before		after	
source (pol)	target (e-t)	source (pol)	target (e-t)
ϕ^+	ϕ^+	ϕ^+	ϕ^+
ϕ^+	ψ^+	ϕ^+	ψ^+
ϕ^+	ϕ^-	ϕ^-	ϕ^-
ϕ^+	ψ^-	ϕ^-	ψ^-
ψ^+	ϕ^+	ψ^+	ψ^+
ψ^+	ψ^+	ψ^+	ϕ^+
ψ^+	ϕ^-	ψ^-	ψ^-
ψ^+	ψ^-	ψ^-	ϕ^-
ϕ^-	ϕ^+	ϕ^-	ϕ^+
ϕ^-	ψ^+	ϕ^-	ψ^+
ϕ^-	ϕ^-	ϕ^+	ϕ^-
ϕ^-	ψ^-	ϕ^+	ψ^-
ψ^-	ϕ^+	ψ^-	ψ^+
ψ^-	ψ^+	ψ^-	ϕ^+
ψ^-	ϕ^-	ψ^+	ψ^-
ψ^-	ψ^-	ψ^+	ϕ^-

seen as parity measurement in some sense. If the measurement results are correlated, meaning the target state is in a ϕ state, the states before the bCNOT were either both in a ϕ or both in a ψ state. If the measurement results are anti-correlated, the states before the bCNOT were either in a ϕ and a ψ or in a ψ and a ϕ state.

Some more patterns can be found in Table A.1. The target state is left invariant if the source was in a ϕ state and the target state experiences a bit flip if the source was in a ψ state. The source state, in turn, is left invariant if the target state was in a ϕ^+ or in a ψ^+ state. If the target state was in a ϕ^- or in a ψ^- state, the source state experiences back-action and the phase is flipped.

A.3 Noisy polarisation channel

A general rotation on the Bloch sphere by an angle θ about a vector $\mathbf{n}$ can be described as

$$R_{\mathbf{n}}(\theta) = \exp\left(-\mathrm{i}\,\frac{\theta}{2}\mathbf{n}\cdot\boldsymbol{\sigma}\right) , \tag{A.3}$$

where $\boldsymbol{\sigma} = (\sigma_\mathrm{x}, \sigma_\mathrm{y}, \sigma_\mathrm{z})^\mathrm{T}$ is a vector with the Pauli matrices as elements. The rotations along the cartesian axes are then

$$R_\mathrm{x}(\theta) = \mathrm{e}^{-\mathrm{i}\frac{\theta}{2}\sigma_\mathrm{x}} = \cos\left(\frac{\theta}{2}\right)\mathbb{1} - \mathrm{i}\sin\left(\frac{\theta}{2}\right)\sigma_\mathrm{x} = \begin{pmatrix} \cos\frac{\theta}{2} & -\mathrm{i}\sin\frac{\theta}{2} \\ -\mathrm{i}\sin\frac{\theta}{2} & \cos\frac{\theta}{2} \end{pmatrix}, \tag{A.4}$$

$$R_\mathrm{y}(\theta) = \mathrm{e}^{-\mathrm{i}\frac{\theta}{2}\sigma_\mathrm{y}} = \cos\left(\frac{\theta}{2}\right)\mathbb{1} - \mathrm{i}\sin\left(\frac{\theta}{2}\right)\sigma_\mathrm{y} = \begin{pmatrix} \cos\frac{\theta}{2} & -\sin\frac{\theta}{2} \\ \sin\frac{\theta}{2} & \cos\frac{\theta}{2} \end{pmatrix}, \tag{A.5}$$

$$R_\mathrm{z}(\theta) = \mathrm{e}^{-\mathrm{i}\frac{\theta}{2}\sigma_\mathrm{z}} = \cos\left(\frac{\theta}{2}\right)\mathbb{1} - \mathrm{i}\sin\left(\frac{\theta}{2}\right)\sigma_\mathrm{x} = \begin{pmatrix} \mathrm{e}^{-\mathrm{i}\frac{\theta}{2}} & 0 \\ 0 & \mathrm{e}^{\mathrm{i}\frac{\theta}{2}} \end{pmatrix}. \tag{A.6}$$

These rotations can be reproduced precisely by the HQHQ channel. For practical purposes the angles of the wave plates are chosen, such that the rotations are mimicked up to the action of a half-wave plate set at 0.

$$Q_0 H_\vartheta Q_0 H_0 = \begin{pmatrix} \cos 2\vartheta & \mathrm{i}\sin 2\vartheta \\ -\mathrm{i}\sin 2\vartheta & -\cos 2\vartheta \end{pmatrix} = R_\mathrm{x}(4\vartheta)\, H_0\,, \tag{A.7}$$

$$Q_{\frac{\pi}{4}} H_{\frac{\pi}{4}-\vartheta} Q_{\frac{\pi}{4}} H_0 = \begin{pmatrix} \cos 2\vartheta & \sin 2\vartheta \\ \sin 2\vartheta & -\cos 2\vartheta \end{pmatrix} = R_\mathrm{y}(4\vartheta)\, H_0\,, \tag{A.8}$$

$$Q_0 H_0 Q_0 H_\vartheta = \begin{pmatrix} \mathrm{e}^{-2\mathrm{i}\,\vartheta} & 0 \\ 0 & -\mathrm{e}^{2\mathrm{i}\,\vartheta} \end{pmatrix} = R_\mathrm{z}(4\vartheta)\, H_0\,. \tag{A.9}$$

A.4 Double Franson interferometer

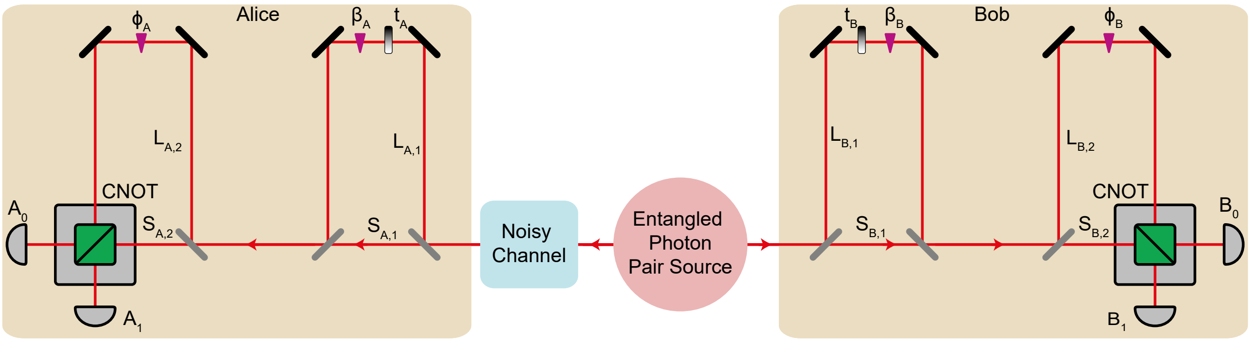

Figure A.1: *Setup including bit flip interferometer with transmission modulator in the long paths.*

To introduce a tunable bit flip error in the e-t DOF, two concatenated Franson interferometers as shown in Figure A.1 may be used. The output state of the first interferometer is

$$|\psi\rangle_{\mathrm{out},1} = \frac{1}{2}\left(|\mathrm{S}\rangle_{\mathrm{A}} + \mathrm{e}^{i\beta_{\mathrm{A}}}\sqrt{t_{\mathrm{A}}}|\mathrm{L}\rangle_{\mathrm{A}}\right) \otimes \frac{1}{2}\left(|\mathrm{S}\rangle_{\mathrm{B}} + \mathrm{e}^{i\beta_{\mathrm{B}}}\sqrt{t_{\mathrm{B}}}|\mathrm{L}\rangle_{\mathrm{B}}\right) \tag{A.10}$$

$$= \frac{1}{4}\Big(|\mathrm{SS}\rangle_{\mathrm{AB}} + \mathrm{e}^{i(\beta_{\mathrm{A}}+\beta_{\mathrm{B}})}\sqrt{t_{\mathrm{A}}t_{\mathrm{B}}}|\mathrm{LL}\rangle_{\mathrm{AB}} + \mathrm{e}^{i\beta_{\mathrm{A}}}\sqrt{t_{\mathrm{A}}}|\mathrm{LS}\rangle_{\mathrm{AB}} + \mathrm{e}^{i\beta_{\mathrm{B}}}\sqrt{t_{\mathrm{B}}}|\mathrm{SL}\rangle_{\mathrm{AB}}\Big)\ . \tag{A.11}$$

The normalisation is chosen such that the state is normalised to one before entering the first interferometer. Half of the counts are lost at the second beamsplitters in both, Alice' and Bob's, arms. The output state of the second interferometer only is

$$|\psi\rangle_{\mathrm{out},2} = \frac{1}{2}\Big(|\mathrm{SS}\rangle_{\mathrm{AB}} + \mathrm{e}^{i(\phi_{\mathrm{A}}+\phi_{\mathrm{B}})}|\mathrm{LL}\rangle_{\mathrm{AB}} + \mathrm{e}^{i\phi_{\mathrm{A}}}|\mathrm{LS}\rangle_{\mathrm{AB}} + \mathrm{e}^{i\phi_{\mathrm{B}}}|\mathrm{SL}\rangle_{\mathrm{AB}}\Big)\ . \tag{A.12}$$

The overall output state $|\psi\rangle_{\mathrm{out}} = |\psi\rangle_{\mathrm{out},1} \otimes |\psi\rangle_{\mathrm{out},2}$ lives in a 16 dimensional space. While all components can be coherent, some are distinguishable due to the time delay accumulated in the long paths. By coincidence measurement a six dimensional subspace spanned by $|\mathrm{SSSS}\rangle$, $|\mathrm{SSLL}\rangle$, $|\mathrm{LLSS}\rangle$, $|\mathrm{LLLL}\rangle$, $|\mathrm{LSSL}\rangle$, $|\mathrm{SLLS}\rangle$ is selected. Here the first two labels represent the short (S) and the long (L) path taken in the first interferometer at Alice's and Bob's side respectively. The third and the fourth labels represent the paths taken in the second interferometer. In order to get a symmetric bit flip, it is assumed that $t_{\mathrm{A}} = t_{\mathrm{B}} \equiv t$.

The fidelity with respect to the Bell states is computed by projecting onto

$$|\phi^+\rangle : \quad \frac{1}{2}\left(|\mathrm{SS}\rangle + |\mathrm{LL}\rangle\right) \otimes \left(|\mathrm{SS}\rangle + |\mathrm{LL}\rangle\right)\ , \tag{A.13}$$

$$|\phi^-\rangle : \quad \frac{1}{2}\left(|\mathrm{SS}\rangle + |\mathrm{LL}\rangle\right) \otimes \left(|\mathrm{SS}\rangle - |\mathrm{LL}\rangle\right)\ , \tag{A.14}$$

$$|\psi^+\rangle : \quad \frac{1}{\sqrt{2}}\left(|\mathrm{SLLS}\rangle + |\mathrm{LSSL}\rangle\right)\ , \tag{A.15}$$

$$|\psi^-\rangle : \quad \frac{1}{\sqrt{2}}\left(|\mathrm{SLLS}\rangle - |\mathrm{LSSL}\rangle\right)\ . \tag{A.16}$$

Here, only the state after the second interferometer is of interest. For the $|\phi^\pm\rangle$ states the relative phase of the terms at the first interferometer is chosen as $+1$ as this is the output state in the used ports (see [71]). The resulting fiedlities are

$$F_{\phi^+} = \frac{1}{32}\left(1 + t^2 + 2t\cos\left(\beta_\mathrm{A} + \beta_\mathrm{B}\right)\right)\cos^2\left(\frac{\phi_\mathrm{A} + \phi_\mathrm{B}}{2}\right), \tag{A.17}$$

$$F_{\phi^-} = \frac{1}{32}\left(1 + t^2 + 2t\cos\left(\beta_\mathrm{A} + \beta_\mathrm{B}\right)\right)\sin^2\left(\frac{\phi_\mathrm{A} + \phi_\mathrm{B}}{2}\right), \tag{A.18}$$

$$F_{\psi^+} = \frac{1}{16}t\cos^2\left(\frac{\beta_\mathrm{A} - \beta_\mathrm{B} - \phi_\mathrm{A} + \phi_\mathrm{B}}{2}\right), \tag{A.19}$$

$$F_{\psi^-} = \frac{1}{16}t\sin^2\left(\frac{\beta_\mathrm{A} - \beta_\mathrm{B} - \phi_\mathrm{A} + \phi_\mathrm{B}}{2}\right). \tag{A.20}$$

The contributions of the central peak and the first two side peaks are shown in Table A.2. The two side peaks with time delay ±2 both contain only one term, that is $\mathrm{e}^{i(\beta_\mathrm{B}+\phi_\mathrm{B})}\sqrt{t}|\mathrm{SLSL}\rangle$ for T_{-2} and $\mathrm{e}^{i(\beta_\mathrm{A}+\phi_\mathrm{A})}|\mathrm{LSLS}\rangle$ for T_2 .

Table A.2: *Output after concatenated Franson interferometers, ordered by relative time delay. Style of timing analysis inspired by [72]*

	T_{-1}		T_0		T_1
$\mathrm{e}^{i\phi_\mathrm{B}}$	$\|\mathrm{SSSL}\rangle$		$\|\mathrm{SSSS}\rangle$	$\mathrm{e}^{i\phi_\mathrm{A}}$	$\|\mathrm{SSLS}\rangle$
$\mathrm{e}^{i(\beta_\mathrm{A}+\beta_\mathrm{B}+\phi_\mathrm{B})}t$	$\|\mathrm{LLSL}\rangle$	$\mathrm{e}^{i(\phi_\mathrm{A}+\phi_\mathrm{B})}$	$\|\mathrm{SSLL}\rangle$	$\mathrm{e}^{i(\beta_\mathrm{A}+\beta_\mathrm{B}+\phi_\mathrm{A})}t$	$\|\mathrm{LLLS}\rangle$
$\mathrm{e}^{i\beta_\mathrm{B}}\sqrt{t}$	$\|\mathrm{SLSS}\rangle$	$\mathrm{e}^{i(\beta_\mathrm{A}+\beta_\mathrm{B})}t$	$\|\mathrm{LLSS}\rangle$	$\mathrm{e}^{i\beta_\mathrm{A}}\sqrt{t}$	$\|\mathrm{LSSS}\rangle$
$\mathrm{e}^{i(\beta_\mathrm{B}+\phi_\mathrm{A}+\phi_\mathrm{B})}\sqrt{t}$	$\|\mathrm{SLLL}\rangle$	$\mathrm{e}^{i(\beta_\mathrm{A}+\beta_\mathrm{B}+\phi_\mathrm{A}+\phi_\mathrm{B})}t$	$\|\mathrm{LLLL}\rangle$	$\mathrm{e}^{i(\beta_\mathrm{A}+\phi_\mathrm{A}+\phi_\mathrm{B})}$	$\|\mathrm{LSLL}\rangle$
		$\mathrm{e}^{i(\beta_\mathrm{A}+\phi_\mathrm{B})}\sqrt{t}$	$\|\mathrm{LSSL}\rangle$		
		$\mathrm{e}^{i(\beta_\mathrm{B}+\phi_\mathrm{A})}\sqrt{t}$	$\|\mathrm{SLLS}\rangle$		

A.5 Source side peaks

As discussed in section 3.3 the Franson interferometer produces peaks of different time delays. The central peak with zero time delay between the detected single photons is surrounded by two side peaks of $\pm\Delta t$ time delay determined by the imbalance of the MZ interferometers. To keep the number of accidental coincidence counts low, the coincidence window is usually kept narrow. For the controlled introduction of an error in the energy-time DOF though, the coincidence window is widened gradually until the side peaks are fully included. Ideally this affects only the e-t DOF and not the polarisation DOF. Unfortunately, this is not the case, as can be seen in the results presented in section 6. Even during measurements of the input polarisation fidelity sidepeaks are observed. For this measurement the Mach-Zehnder interferometers are turned off by blocking the long arm (ref. section 5.5.1), so no sidepeaks can be produced by the Franson interferometer. The observed sidepeaks are traced back to the source. Here they are observed analysing the polarisation with a Bob module connected via single-mode fibre. The side peaks always contain the unwanted correlations, which are minimal in the central peak. Maximising the state, and so the central peak, on correlated coincidences leads to maximised anti-correlated coincidences in the side peaks. Similarly correlated coincidences are maximal in the side if anti-correlated coincidences are maximal in the central peak. Reflections at the long pass filter and in the single-mode fibre have been excluded by tilting or replacing them. The side peaks vanish when the polarisation is analysed with polarisers in front of the collimators for the single photons. From this, it is assumed that the side peaks arise from a reflection at the collimator. The photons travel back to the loop, pass the HWP in the loop and are so directed back to the collimator they were reflected from but with orthogonal polarisation. This is why they cannot pass the polariser a third time.

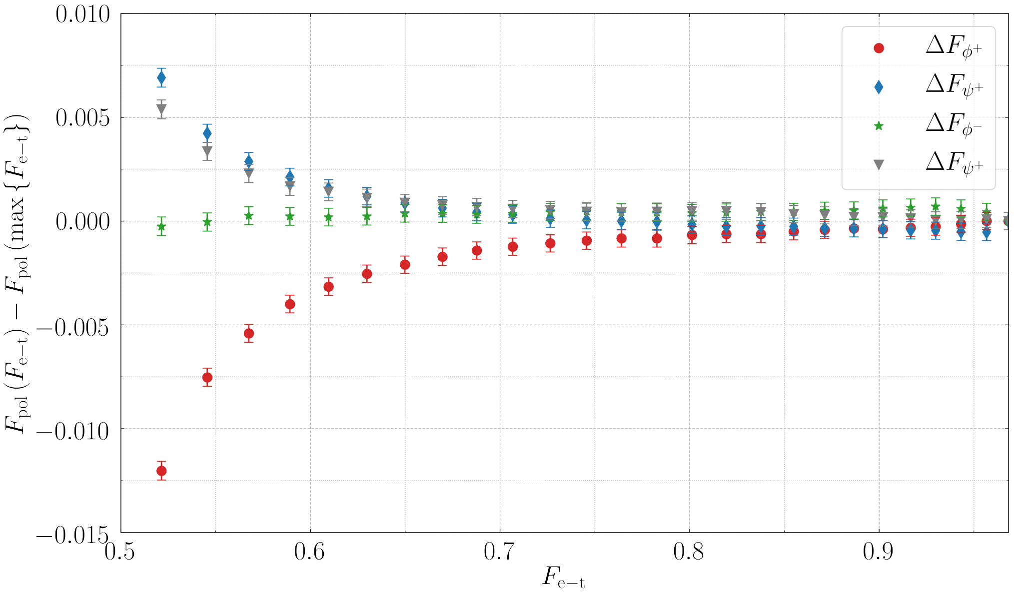

Figure A.2: *Crosstalk between the polarisation and the energy-time DOF. The deviation of the fidelities is given with respect to a narrow coincidence window that corresponds to the maximal energy-time fidelity. The noisy channel is fixed at the neutral position. By widening the coincidence window the e-t fidelity decreases, but at some point also the polarisation fidelity with respect to the* ϕ^+ *state decreases. This is caused by the source side peaks discussed in the text.*

The side peaks have not been a problem for experiments that used this source before as the coincidence window has been small enough to exclude the side peaks at all times. In this distillation experiment, however, widening the coincidence window is essential and so the side peaks caused by reflections in the source which occur at a similar time delay as the side peaks of the Franson interferometer cannot be avoided. As the path length difference in the Franson interferometer is chosen carefully and should not be changed and the collimator cannot be tilted, the only option would be to increase the distance between the Sagnac loop and the collimators. This would decrease the stability of the source due to more sensitive coupling to the single-mode fibres. In addition, the couplers would have to be positioned on a different breadboard and the acrylic box for passive stabilization would have to be extended.

Bibliography

[1] Lov K. Grover. Quantum mechanics helps in searching for a needle in a haystack. *Phys. Rev. Lett.*, 79:325, 1997.

[2] Lov K. Grover. A fast quantum mechanical algorithm for database search. In *Proceedings of the Twenty-Eighth Annual ACM Symposium on Theory of Computing*, STOC '96, pages 212–219, New York, NY, USA, 1996. Association for Computing Machinery.

[3] P. W. Shor. Algorithms for quantum computation: discrete logarithms and factoring. In *Proceedings 35th Annual Symposium on Foundations of Computer Science*, pages 124–134, 1994.

[4] Peter W. Shor. Polynomial-time algorithms for prime factorization and discrete logarithms on a quantum computer. *SIAM Review*, 41(2):303, 1999.

[5] Eleni Diamanti, Hoi-Kwong Lo, Bing Qi, and Zhiliang Yuan. Practical challenges in quantum key distribution. *npj Quantum Information*, 2(1):16025, 2016.

[6] W. K. Wootters and W. H. Zurek. A single quantum cannot be cloned. *Nature*, 299(5886):802, 1982.

[7] Michael A. Nielsen and Isaac L. Chuang. *Quantum Computation and Quantum Information: 10th Anniversary Edition.* Cambridge University Press, 2010.

[8] Charles H. Bennett, Gilles Brassard, Sandu Popescu, Benjamin Schumacher, John A. Smolin, and William K. Wootters. Purification of noisy entanglement and faithful teleportation via noisy channels. *Phys. Rev. Lett.*, 76:722, 1996.

[9] Charles H. Bennett, David P. DiVincenzo, John A. Smolin, and William K. Wootters. Mixed-state entanglement and quantum error correction. *Phys. Rev. A*, 54:3824, 1996.

[10] Charles H. Bennett, Gilles Brassard, Claude Crépeau, Richard Jozsa, Asher Peres, and William K. Wootters. Teleporting an unknown quantum state via dual classical and einstein-podolsky-rosen channels. *Phys. Rev. Lett.*, 70:1895, 1993.

[11] Dik Bouwmeester, Jian-Wei Pan, Klaus Mattle, Manfred Eibl, Harald Weinfurter, and Anton Zeilinger. Experimental quantum teleportation. *Nature*, 390(6660):575, 1997.

[12] W. Dür, H.-J. Briegel, J. I. Cirac, and P. Zoller. Quantum repeaters based on entanglement purification. *Phys. Rev. A*, 59:169, 1999.

[13] Jian-Wei Pan, Dik Bouwmeester, Harald Weinfurter, and Anton Zeilinger. Experimental entanglement swapping: Entangling photons that never interacted. *Phys. Rev. Lett.*, 80:3891, 1998.

[14] David Deutsch, Artur Ekert, Richard Jozsa, Chiara Macchiavello, Sandu Popescu, and Anna Sanpera. Quantum privacy amplification and the security of quantum cryptography over noisy channels. *Phys. Rev. Lett.*, 77:2818, 1996.

[15] Michal Horodecki, Pawel Horodecki, and Ryszard Horodecki. Distillability of inseparable quantum systems, 1996.

[16] Charles H. Bennett, Herbert J. Bernstein, Sandu Popescu, and Benjamin Schumacher. Concentrating partial entanglement by local operations. *Phys. Rev. A*, 53:2046, 1996.

[17] N. Gisin. Hidden quantum nonlocality revealed by local filters. *Physics Letters A*, 210(3):151, 1996.

[18] Claude Cohen-Tannoudji. *Quantum mechanics : 1.* Textbook physics. Wiley Hermann, New York, NY Paris, 2., rev. and enl. ed., [repr.]. edition, 2005.

[19] Stephen M Barnett. *Quantum information.* Oxford master series in atomic, optical and laser physics ; 16. Oxford Univ. Pr., Oxford, 1. publ. edition, 2009.

[20] Jun J Sakurai. *Modern quantum mechanics.* Pearson new international edition. Pearson, Harlow, Essex, 2. edition, 2014.

[21] Ingemar Bengtsson and Karol Zyczkowski. *Geometry of Quantum States: An Introduction to Quantum Entanglement.* Cambridge University Press, 2006.

[22] Reinhard F. Werner. Quantum states with einstein-podolsky-rosen correlations admitting a hidden-variable model. *Phys. Rev. A*, 40:4277, 1989.

[23] Ryszard Horodecki, Paweł Horodecki, Michał Horodecki, and Karol Horodecki. Quantum entanglement. *Rev. Mod. Phys.*, 81:865, 2009.

[24] Anton Zeilinger. *A Foundational Principle for Quantum Mechanics*, pages 235–245. Springer International Publishing, Cham, 2019.

[25] E. Collett. *Field Guide to Polarization.* Field Guide Series. SPIE Press, 2005.

[26] Bahaa E Saleh. *Fundamentals of photonics.* Wiley series in pure and applied optics. Wiley, New York, NY, 2. edition, 2007.

[27] Anthony Mark Fox. *Quantum optics : an introduction.* Oxford master series in physics ; 15 : Atomic, optical and laser physics. Oxford Univ. Pr., Oxford, 1. publ. edition, 2006.

[28] Zhe-Yu Jeff Ou. *Quantum optics for experimentalists.* World Scientific, New Jersey London Singapore Beijing Shanghai Hong Kong Taipei Chennai Tokyo, 2017.

[29] Paul G. Kwiat, Klaus Mattle, Harald Weinfurter, Anton Zeilinger, Alexander V. Sergienko, and Yanhua Shih. New high-intensity source of polarization-entangled photon pairs. *Phys. Rev. Lett.*, 75:4337, 1995.

[30] Ali Anwar, Chithrabhanu Perumangatt, Fabian Steinlechner, Thomas Jennewein, and Alexander Ling. Entangled photon-pair sources based on three-wave mixing in bulk crystals, 2020.

[31] E. Hecht. *Optics, Global Edition.* Pearson Education Limited, 2016.

[32] Robert W. Boyd. *Nonlinear optics.* Academic Press, Amsterdam; Boston, 3. edition, 2008.

[33] Taehyun Kim, Marco Fiorentino, and Franco N. C. Wong. Phase-stable source of polarization-entangled photons using a polarization sagnac interferometer. *Phys. Rev. A*, 73:012316, 2006.

[34] Alessandro Fedrizzi, Thomas Herbst, Andreas Poppe, Thomas Jennewein, and Anton Zeilinger. A wavelength-tunable fiber-coupled source of narrowband entangled photons. *Opt. Express*, 15(23):15377, 2007.

[35] Hiroki Takesue and Kaoru Shimizu. Effects of multiple pairs on visibility measurements of entangled photons generated by spontaneous parametric processes. *Optics Communications*, 283(2):276, 2010.

[36] Paul G. Kwiat. Hyper-entangled states. *Journal of Modern Optics*, 44(11-12):2173, 1997.

[37] J. D. Franson. Bell inequality for position and time. *Phys. Rev. Lett.*, 62:2205, 1989.

[38] Z. Y. Ou, X. Y. Zou, L. J. Wang, and L. Mandel. Observation of nonlocal interference in separated photon channels. *Phys. Rev. Lett.*, 65:321, 1990.

[39] J. G. Rarity and P. R. Tapster. Experimental violation of bell's inequality based on phase and momentum. *Phys. Rev. Lett.*, 64:2495, 1990.

[40] J. D. Franson. Two-photon interferometry over large distances. *Phys. Rev. A*, 44:4552, 1991.

[41] J Brendel, E Mohler, and W Martienssen. Experimental test of bell's inequality for energy and time. *Europhysics Letters (EPL)*, 20(7):575, 1992.

[42] P. G. Kwiat, A. M. Steinberg, and R. Y. Chiao. High-visibility interference in a bell-inequality experiment for energy and time. *Phys. Rev. A*, 47:R2472, 1993.

[43] P. R. Tapster, J. G. Rarity, and P. C. M. Owens. Violation of bell's inequality over 4 km of optical fiber. *Phys. Rev. Lett.*, 73:1923, 1994.

[44] R Y Chiao, P G Kwia, and A M Steinberg. Quantum non-locality in two-photon experiments at berkeley. *Quantum and Semiclassical Optics: Journal of the European Optical Society Part B*, 7(3):259, 1995.

[45] D. V. Strekalov, T. B. Pittman, A. V. Sergienko, Y. H. Shih, and P. G. Kwiat. Postselection-free energy-time entanglement. *Phys. Rev. A*, 54:R1, 1996.

[46] Julio T. Barreiro, Nathan K. Langford, Nicholas A. Peters, and Paul G. Kwiat. Generation of hyperentangled photon pairs. *Phys. Rev. Lett.*, 95:260501, 2005.

[47] Paul G. Kwiat and Harald Weinfurter. Embedded bell-state analysis. *Phys. Rev. A*, 58:R2623, 1998.

[48] Carsten Schuck, Gerhard Huber, Christian Kurtsiefer, and Harald Weinfurter. Complete deterministic linear optics bell state analysis. *Phys. Rev. Lett.*, 96:190501, 2006.

[49] Julio T. Barreiro, Tzu-Chieh Wei, and Paul G. Kwiat. Erratum: Beating the channel capacity limit for linear photonic superdense coding. *Nature Physics*, 4(8):662, 2008.

[50] Brian P. Williams, Ronald J. Sadlier, and Travis S. Humble. Superdense coding over optical fiber links with complete bell-state measurements. *Phys. Rev. Lett.*, 118:050501, 2017.

[51] Klaus Mattle, Harald Weinfurter, Paul G. Kwiat, and Anton Zeilinger. Dense coding in experimental quantum communication. *Phys. Rev. Lett.*, 76:4656, 1996.

[52] Fabian Steinlechner, Sebastian Ecker, Matthias Fink, Bo Liu, Jessica Bavaresco, Marcus Huber, Thomas Scheidl, and Rupert Ursin. Distribution of high-dimensional entanglement via an intra-city free-space link. *Nature Communications*, 8:15971, 2017. Article.

[53] Sebastian Ecker, Frédéric Bouchard, Lukas Bulla, Florian Brandt, Oskar Kohout, Fabian Steinlechner, Robert Fickler, Mehul Malik, Yelena Guryanova, Rupert Ursin, and Marcus Huber. Overcoming noise in entanglement distribution. *Phys. Rev. X*, 9:041042, 2019.

[54] Frank Verstraete, Jeroen Dehaene, and Bart DeMoor. Local filtering operations on two qubits. *Phys. Rev. A*, 64:010101, 2001.

[55] Paul G. Kwiat, Salvador Barraza-Lopez, André Stefanov, and Nicolas Gisin. Experimental entanglement distillation and 'hidden' non-locality. *Nature*, 409(6823):1014, 2001.

[56] Zhi-Wei Wang, Xiang-Fa Zhou, Yun-Feng Huang, Yong-Sheng Zhang, Xi-Feng Ren, and Guang-Can Guo. Experimental entanglement distillation of two-qubit mixed states under local operations. *Phys. Rev. Lett.*, 96:220505, 2006.

[57] M. Zwerger, H. J. Briegel, and W. Dür. Robustness of hashing protocols for entanglement purification. *Phys. Rev. A*, 90:012314, 2014.

[58] T. B. Pittman, B. C. Jacobs, and J. D. Franson. Probabilistic quantum logic operations using polarizing beam splitters. *Phys. Rev. A*, 64:062311, 2001.

[59] J. L. O'Brien, G. J. Pryde, A. G. White, T. C. Ralph, and D. Branning. Demonstration of an all-optical quantum controlled-not gate. *Nature*, 426(6964):264, 2003.

[60] Sara Gasparoni, Jian-Wei Pan, Philip Walther, Terry Rudolph, and Anton Zeilinger. Realization of a photonic controlled-not gate sufficient for quantum computation. *Phys. Rev. Lett.*, 93:020504, 2004.

[61] Zhi Zhao, An-Ning Zhang, Yu-Ao Chen, Han Zhang, Jiang-Feng Du, Tao Yang, and Jian-Wei Pan. Experimental demonstration of a nondestructive controlled-not quantum gate for two independent photon qubits. *Phys. Rev. Lett.*, 94:030501, 2005.

[62] Jian-Wei Pan, Christoph Simon, Caslav Brukner, and Anton Zeilinger. Entanglement purification for quantum communication. *Nature*, 410(6832):1067, 2001.

[63] Christoph Simon and Jian-Wei Pan. Polarization entanglement purification using spatial entanglement. *Phys. Rev. Lett.*, 89:257901, 2002.

[64] Jian-Wei Pan, Sara Gasparoni, Rupert Ursin, Gregor Weihs, and Anton Zeilinger. Experimental entanglement purification of arbitrary unknown states. *Nature*, 423(6938):417, 2003.

[65] P. Walther, K. J. Resch, Č. Brukner, A. M. Steinberg, J.-W. Pan, and A. Zeilinger. Quantum nonlocality obtained from local states by entanglement purification. *Phys. Rev. Lett.*, 94:040504, 2005.

[66] Xi-Han Li. Deterministic polarization-entanglement purification using spatial entanglement. *Phys. Rev. A*, 82:044304, 2010.

[67] Sören Wengerowsky, Siddarth Koduru Joshi, Fabian Steinlechner, Julien R. Zichi, Sergiy M. Dobrovolskiy, René van der Molen, Johannes W. N. Los, Val Zwiller, Marijn A. M. Versteegh, Alberto Mura, Davide Calonico, Massimo Inguscio, Hannes Hübel, Liu Bo, Thomas Scheidl, Anton Zeilinger, André Xuereb, and Rupert Ursin. Entanglement distribution over a 96-km-long submarine optical fiber. *Proceedings of the National Academy of Sciences*, 116(14):6684, 2019.

[68] I. Marcikic, H. de Riedmatten, W. Tittel, H. Zbinden, M. Legré, and N. Gisin. Distribution of time-bin entangled qubits over 50 km of optical fiber. *Phys. Rev. Lett.*, 93:180502, 2004.

[69] Sebastian Ecker, Philipp Sohr, Lukas Bulla, Marcus Huber, Martin Bohmann, and Rupert Ursin. Experimental single-copy entanglement distillation, 2021.

[70] Xiao-Min Hu, Cen-Xiao Huang, Yu-Bo Sheng, Lan Zhou, Bi-Heng Liu, Yu Guo, Chao Zhang, Wen-Bo Xing, Yun-Feng Huang, Chuan-Feng Li, and Guang-Can Guo. Long-distance entanglement purification for quantum communication. *Phys. Rev. Lett.*, 126:010503, 2021.

[71] Paul Gregory Kwiat. *Nonclassical Effects from Spontaneous Parametric Down-Conversion Adventures in Quantum Wonderland.* PhD thesis, UNIVERSITY OF CALIFORNIA, BERKELEY., 1993. Ch.8 p. 125 (150): Franson experiment.

[72] A. Martin, F. Kaiser, A. Vernier, A. Beveratos, V. Scarani, and S. Tanzilli. Cross time-bin photonic entanglement for quantum key distribution. *Phys. Rev. A*, 87:020301, 2013.